A nucleotide resolution map of Top2-linked DNA breaks in the yeast and human genome

William Gittens, Dominic J. Johnson, Rachal M. Allison, Tim J. Cooper, Holly Thomas, and Matthew J Neale

Genome Damage and Stability Centre, University of Sussex, UK, BN1 9RQ

Corresponding author: m.neale@sussex.ac.uk

Abstract

DNA topoisomerases are required to resolve DNA topological stress. Despite this essential role, abortive topoisomerase activity generates aberrant protein-linked DNA breaks, jeopardising genome stability. Here, to understand the genomic distribution and mechanisms underpinning topoisomerase-induced DNA breaks, we map Top2 DNA cleavage with strand-specific nucleotide resolution across the *S. cerevisiae* and human genomes—and use the meiotic Spo11 protein to validate the broad applicability of this method to explore the role of diverse topoisomerase family members. Our data characterises Mre11-dependent repair in yeast, and defines two strikingly different fractions of Top2 activity in humans: tightly localised CTCF-proximal and broadly distributed transcription-proximal. Moreover, the nucleotide resolution accuracy of our assay reveals the influence primary DNA sequence has upon Top2 cleavage—for the first time distinguishing canonical DNA double-strand breaks (DSBs) from a major population of DNA single-strand breaks (SSBs) induced by etoposide (VP16) *in vivo*.

Introduction

DNA topoisomerases are a broad and ubiquitous family of enzymes that tackle topological constraints to replication, transcription, the maintenance of genome structure and chromosome segregation in mitosis and meiosis (Pommier et al., 2016). Although the specific mechanisms by which this is accomplished vary considerably across the family, key aspects are shared: including single or double-strand DNA cleavage to form a transient covalent complex (CC), which allows alteration of the topology of the nucleic acid substrate prior to relegation (Wang, 2009). These processes are essential but carry with them a significant risk to genome stability because the CC may be stabilised as a permanent

protein-linked DNA break by several physiological factors; such as the proximity of other DNA lesions (Sabourin and Osheroff, 2000; Kingma et al., 1995; Khan et al., 2003; Vélez-Cruz et al., 2005; Deweese and Osheroff, 2009; Wang et al., 2000; Wang et al., 1999), the collision of transcription and replication complexes (Wu and Liu, 1997; Hsiang et al., 1989), denaturation of the topoisomerase (Liu et al., 1983), or by the binding of small molecules that inhibit religation (Reviewed in (Nitiss, 2009)). Topoisomerase-induced DNA strand breaks have been proposed to constitute a significant fraction of the total damage to genomic DNA per day, and have been linked to the genesis and development of various cancers (Lin et al., 2009; Haffner et al., 2010; Sasanuma et al., 2018), including a subset of therapy-related acute myeloid leukaemias (t-AML) caused by the use of Topoisomerase 2 (Top2) poisons in the chemotherapeutic treatment of primary cancers (Rowley and Olney, 2002; Cowell et al., 2012).

In *S. cerevisiae*, either Top1 or Top2 activity is sufficient to support transcription (Brill et al., 1987; Lotito et al., 2008; Bermejo et al., 2009). However, whilst *top1*Δ cells are viable, Top2 is essential for sister chromatid segregation (Baxter and Diffley, 2008; DiNardo et al., 1984; Holm et al., 1985; Uemura and Yanagida, 1984). In contrast to *S. cerevisiae*, all known vertebrate species encode two Top2 proteins (TOP2α and TOP2β). Interestingly, whilst TOP2α is essential for cellular proliferation—cells arrest in mitosis in its absence (Akimitsu et al., 2003)—TOP2β is not. Rather, TOP2β apparently plays an important role in promoting transcriptional programmes associated with neuronal development (Tiwari et al., 2012; Gómez-Herreros et al., 2014), a function that cannot be supported by TOP2α.

Accurate maps of the positions of topoisomerase-DNA covalent complexes (Top2 CCs) genome-wide and throughout the cell cycle provide insights into topological genome structural organisation, as well as providing the tools to study their repair should they become permanent DNA lesions. Whilst the dual catalytic sites present within the homodimeric Top2 enzyme suggest a primary role in DNA double-strand break (DSB) formation driven by a biological need for decatenation (Pommier et al., 2016), previous research has suggested that etoposide and other Top2 poisons may induce a population of DNA single-strand breaks (SSBs), due to independent inhibition of each active site (Wozniak and Ross, 1983; Long et al., 1986; Zwelling et al., 1981; Pommier et al., 1984; Bromberg et al., 2003). Yet, despite the use of etoposide in chemotherapy, and the different toxicity of these two classes of DNA lesion, the prevalence of Top2-SSBs remains unclear.

More recently, general DSB mapping techniques have been applied to map etoposide-induced lesions (Canela et al., 2017; Crosetto et al., 2013; Yan et al., 2017). However, such methods are only able to map DSB ends, which therefore excludes and obscures etoposide-induced SSBs. Moreover, these methodologies lack specificity for protein-linked DNA ends, and require nucleolytic processing to blunt 5' DNA termini as part of sample preparation (Canela et al., 2017). When combined, these factors lead to loss of nucleotide resolution at the site of Top2 cleavage.

To generate a more complete, and direct, picture of topoisomerase action across the genome, we present here a technique for nucleotide resolution mapping of protein-linked SSBs and DSBs (referred to collectively here as "Covalent Complexes"; CC), which we demonstrate to be generally applicable in both yeast and human cell systems. We establish with high confidence that the technique is able to map both the positions of Top2 CCs and also CCs of DNA linked to the meiotic recombination protein Spo11, which is related to the archaeal Topoisomerase VI (Bergerat et al., 1997). Furthermore, we provide insights into the spatial distribution of human TOP2 CCs, including comparative analysis of their local enrichment around transcription start sites (TSSs) and CTCF-binding motifs. We find that TSS-proximal TOP2 CC levels are strongly correlated with transcription, a question that has come under scrutiny recently (Canela et al., 2017). Finally, we present compelling evidence that etoposide induces a majority of Top2-linked SSBs *in vivo*, corroborating previous research and revealing, for the first time, that this is governed by primary DNA sequence at the cleavage site.

Results

CC-seq enriches Spo11-linked DNA fragments

To elucidate the *in vivo* functions of topoisomerase-like enzymes, we set out to establish a direct method (termed 'CC-seq') to enrich and map protein-DNA covalent complexes (CC) genome-wide with nucleotide resolution. Silica fibre-based enrichment of CCs has been used to study the adenovirus DNA terminal protein complex (Coombs and Pearson, 1978), and in the original identification of the meiotic DSB-inducer Spo11 (Keeney and Kleckner, 1995; Keeney et al., 1997), an orthologue of archaeal Topoisomerase VI (Bergerat et al., 1997). We first verified this enrichment principle using meiotic *sae2*Δ cells, in which Spo11-linked DSBs are known to accumulate at defined loci due to abrogation of the nucleolytic pathway that releases Spo11 (Keeney and Kleckner, 1995; Neale et al., 2005). To demonstrate specific enrichment of protein-linked molecules, total genomic DNA from

meiotic *S. cerevisiae* cells was isolated in the absence of proteolysis, digested with *Pst*I restriction enzyme, and isolated on glass-fibre spin columns (**Figure 1A, Methods**). We used eluted material to assay a known Spo11-DSB hotspot by Southern blotting (**Figure 1B**). While DSB fragments are a minor fraction of input material (~10% of total), and were absent in wash fractions, DSBs accounted for >99% of total eluted material, indicating ~1000-fold enrichment relative to non-protein-linked DNA (**Figure 1B**).

CC-seq maps known Spo11-DSB hotspots genome-wide with high reproducibility

To generate a genome-wide map of Spo11-DSBs, genomic DNA from meiotic *sae2*Δ cells was sonicated to <400 bp in length, enriched upon the silica column, eluted, and ligated to DNA adapters in a two-step procedure that utilised the known phosphotyrosyl-unlinking activity of mammalian TDP2 to uncap the Spo11-bound end ('CC-seq'; **Figure 1A / Methods**) (Cortes Ledesma et al., 2009; Johnson et al., 2019). Libraries were paired-end sequenced and mapped to the *S. cerevisiae* reference genome (**Table S1**) alongside reads from a previous mapping technique ('Spo11-oligo-seq') that relies on the isolation of Spo11-linked oligonucleotides generated in wild-type cells during DSB repair (Pan et al., 2011). CC-seq revealed sharp, localised peaks ('hotspots') in *SPO11*+ cells (**Figure 1C, middle**) that visually (**Figure 1C**) and quantitatively (**Figure 1S1A**, r=0.82) correlate with Spo11-oligo seq, and that are absent in the *spo11-Y135F* control strain (**Figure 1C, bottom**) in which Spo11-DSBs do not form (Bergerat et al., 1997), demonstrating that signal detected by CC-seq accurately reflects the distribution of Spo11 cleavages. Moreover, CC-seq maps generated from independent biological samples were highly correlated (**Figure S1B**; r = 0.98), demonstrating very high reproducibility. Finally, when analysed at nucleotide resolution, CC-seq revealed high correlation (r = 0.85) between the frequency of Watson-mapping and Crick-mapping cleavage sites, when offset by a single bp (**Figure 1E and S1C**). This correlation is expected because of the 2 bp 5' overhang generated at Spo11-DSBs *in vivo* (**Fig1D**; e.g. (Liu et al., 1995))—demonstrating the nucleotide resolution accuracy of CC-seq, which is further supported by our observation of nucleotide composition preference at the site of cleavage (**Figure 1E**).

CC-seq enriches and maps Top2-linked DNA fragments from *S. cerevisiae*

Confident in the specificity of CC-seq to map meiotic protein-linked DSBs with high resolution and dynamic range, we next employed CC-seq to map within *S. cerevisiae* the covalent complexes generated naturally by Topoisomerase 2 (Top2) that become stabilised upon exposure to etoposide, and are thus a proxy for sites of Top2 catalytic activity

142 (Minocha and Long, 1984; Chen et al., 1984; Wu et al., 2011). Because *S. cerevisiae* is
143 relatively insensitive to etoposide, we utilised a strain background ('*pdr1*Δ') in which the
144 action of the major drug export pathways are downregulated due to modulation of *PDR1*
145 activity (Stepanov et al., 2008). As expected, the *pdr1*Δ background dramatically increased
146 cellular sensitivity to etoposide, which was further enhanced by mutation of *SAE2* and
147 *MRE11* (**Figure 2A**), factors involved in the repair of covalent protein-linked DNA breaks
148 (Neale et al., 2005; Garcia et al., 2011; Anand et al., 2016; Cannavo and Cejka, 2014;
149 Cannavo et al., 2018; Hoa et al., 2016; Hartsuiker et al., 2009).
150
151 Next, we prepared sequencing libraries from mitotically growing etoposide-treated control
152 (*pdr1*Δ) *S. cerevisiae* cells, or cells that also harboured *sae2*Δ and *mre11*Δ mutations (**Table**
153 **S2**). A human DNA spike-in was included to enable calibration of relative signal between
154 strains (**Methods**). Libraries displayed high replicate-to-replicate reproducibility (r = 0.89,
155 0.95 and 0.97 for control, *sae2*Δ and *mre11*Δ, respectively; **Figures S2A-C**), therefore
156 replicates were pooled. In untreated control cells, Top2 CC signal was distributed
157 homogeneously across the genome, with few strong peaks (**Figure 2B**). Upon etoposide
158 treatment, sharp single-nucleotide peaks arose at similar locations across the genome in all
159 strains (**Figure 2B and S2D-E**), but with increased amplitude in the repair mutants—thereby
160 directly linking the MRX pathway to repair of Top2 CCs in *S. cerevisiae*, and corroborating
161 prior research in other organisms (Hartsuiker et al., 2009; Hoa et al., 2016; Nakamura et al.,
162 2010).
163
164 Global analyses revealed Top2 activity in *S. cerevisiae* to be relatively enriched in divergent
165 and tandem intergenic regions (IGRs) and depleted in intragenic and convergent IGRs
166 (**Figure 2B and C**), similar to, but less pronounced than, the patterns of Spo11 (**Figure 2B**
167 **and C**). Such connections to global gene organisation are likely driven by the need for
168 Spo11 and Top2 to interact with the DNA helix—an interpretation underpinned by an
169 anticorrelation with nucleosome occupancy (**Figure S1E and S3A**). Nevertheless, the fact
170 that *S. cerevisiae* Top2 CC signal is not correlated with proximal gene expression—neither
171 in untreated cells, nor following etoposide exposure (**Figure S3B**)—suggests that in the
172 gene-dense *S. cerevisiae* genome topological stress may be dealt with by Top2 at sites
173 dislocated from where it is generated. By contrast, Spo11 activity is positively correlated
174 with gene expression (**Figure S1D**), perhaps due to the influence transcription has upon the
175 generation of higher order chromatin loop structures (Schalbetter et al., 2018), which in turn
176 are known to pattern Spo11-DSBs (Sun et al., 2015).

177

178 Interestingly, Top2 CC signal remained weakly correlated over greater distances than
179 Spo11 (**Figure 2D**), suggesting localised 5-10 kb wide regions of enriched activity—much
180 larger than Spo11-DSB hotspots (generally <500 bp in size; **Figure 1C**; (Pan et al., 2011)).
181 Top2 activity was strongly correlated between Watson and Crick strands when offset by 3
182 bp (**Figure 2E and S2F-K**)—as expected for the 4 bp overhang generated by Top2-DSBs—
183 further demonstrating the nucleotide resolution accuracy of CC-seq. Together these data
184 describe how CC-seq reveals a strand-specific nucleotide resolution map of etoposide-
185 induced Top2 CCs.

186

187 **CC-seq maps TOP2 CCs in the Human genome**

188 Having demonstrated that CC-seq is applicable for mapping two divergent types of
189 topoisomerase-like covalent complexes in *S. cerevisiae*, we applied CC-seq to map TOP2
190 activity in a human cell system. Asynchronous, sub-confluent RPE-1 cells were treated with
191 etoposide (VP16) in the presence of MG132 proteasome inhibitor, in order to limit potential
192 proteolytic degradation of TOP2 CCs that might otherwise hamper enrichment (**Figure 1A**).
193 Slot-blotting and immunodetection with anti-TOP2β antibody demonstrated complete
194 recovery of input TOP2β-linked CCs within the column elution, with no TOP2β remaining in
195 the flow through or being removed by the washes (**Figure 3A**). Eluted material was used to
196 generate sequencing libraries from three replicate control (–VP16) and four replicate
197 etoposide-treated samples (+VP16), and high-depth paired-end sequencing reads (**Table**
198 **S2**) were aligned to the human genome (hg19; **Methods**).

199

200 Replicates displayed high correlation in the distribution of TOP2 CC signal at broad scale (r
201 values ≥ 0.79; **Figure S4A-B**), and so were pooled. Visual inspection revealed that -VP16
202 and +VP16 signals are spatially-correlated (**Figure 3B**), but that +VP16 signal intensity is
203 less uniform, with more dynamic range (**Figure S4C-D**). These differences are likely due to
204 higher signal-to-noise enabled by enrichment of TOP2 CC following VP16 treatment. Like
205 yeast Top2 libraries (**Figure 2E**), nucleotide resolution analysis of human CC-seq libraries
206 displayed a skew towards Watson-Crick read-pairs that are offset by 3 bp, as expected for
207 the 4 bp 5' overhang generated by TOP2 (**Figure S4E**). This skew is much greater in VP16-
208 treated samples (**Figure S4E**), supporting the view that +VP16 libraries have greater Top2
209 CC enrichment.

210

211 The human genome encodes two type-IIA topoisomerases, TOP2α and TOP2β
212 (**Introduction**). To demonstrate the specificity of CC-seq to map human TOP2 activity we
213 used CRISPR-Cas9 to generate a human RPE-1-derived cell line with homozygous
214 knockout mutations in the non-essential *TOP2B* gene, and arrested cells in G1 (**Figure S5A**)
215 when TOP2α is not expressed (Heck et al., 1988; Woessner et al., 1991; Negri et al., 1992).
216 TOP2α and TOP2β expression was undetectable in such G1-arrested cells (**Figure S5B**),
217 and importantly, VP16-induced γ-H2AX foci were reduced ~7-fold relative to wild type
218 control lines, indicating that most of the signal is TOP2β-dependent (**Figure S5C-D**).
219
220 Next, we applied CC-seq to asynchronous and G1-arrested wild type and *TOP2B*$^{-/-}$ cells. In
221 G1, VP16 exposure induced localised regions of enriched TOP2 CC formation in wild type
222 cells that were largely diminished or absent in *TOP2B*$^{-/-}$ cells (**Figure S5E**). By comparison,
223 TOP2β deletion did not prevent VP16-induced signal in asynchronous cells (**Figure S5E**), in
224 which TOP2α is still present. Together, these results indicate that CC-seq detects a mixture
225 of both TOP2α and TOP2β covalent complexes in wild type human cells depending on the
226 cell cycle phase.
227
228 **Spatial distribution of Top2 activity in the human genome**
229 The human genome is divided into a relatively gene-rich 'A' compartment and a relatively
230 gene-poor 'B' compartment, the 3D spatial segregation of which can be determined by HiC
231 (Lieberman-Aiden et al., 2009). In both untreated and VP16-treated asynchronous wild type
232 cells, TOP2 CC are enriched in the active A compartment (**Figure 3B and C**), consistent
233 with the role of TOP2 in facilitating transcription. TOP2 activity also correlated with regions
234 of negative DNA supercoiling (Naughton et al., 2013) (**Figure 3B**). These observations
235 provide a functional link between TOP2 activity, DNA topological stress, and large-scale
236 chromatin compartments.
237
238 We next focused our attention in more detail on the genome-wide pattern of TOP2 activity
239 enriched by VP16 treatment. Simple visual inspection (**Figure 3D**) suggested that TOP2 CC
240 signals are enriched around genome features previously identified as regions of high TOP2-
241 binding and etoposide-induced DNA strand breakage, including sites of CTCF-binding
242 (Uusküla-Reimand et al., 2016; Canela et al., 2017) and active transcription start sites
243 (TSSs) marked by H3K4Me3 and H3K27Ac (Baranello et al., 2014; Yang et al., 2015).
244

245 Genomic maps of etoposide-induced DNA breaks were recently generated using a related
246 methodology, 'END-seq' (Canela et al., 2017), that is not specific for protein-linked TOP2
247 CC. Aggregating END-seq data around strong CC-seq positions revealed concordant peak
248 signals at broad scale (**Figure 3E**), demonstrating a general agreement in the positions
249 reported by the two techniques. However, at finer scale, END-seq positions are offset by 1-
250 15 bp in the 3' direction relative to CC-seq positions on each strand (**Figure 3F**)—
251 something not observed when aggregating CC-seq data around the same loci (**Figure 3F**).
252 This important difference is likely to be explained by the different populations of DNA
253 breaks mapped by each technique: specific TOP2 cleavage positions (CC-seq) versus DNA
254 breaks that have undergone limited nucleolytic resection (END-seq).
255
256 To investigate the relationship between CTCF and TOP2 activity, we filtered CTCF motifs to
257 include only those that overlapped an RPE-1 CTCF ChIP-seq peak (**Methods;** (Akimitsu et
258 al., 2003)). After aligning Watson and Crick motifs in the same orientation, we frequently
259 observed a strong TOP2 CC peak upstream of the motif centre and accompanied by more
260 distal, weaker peaks on both sides of the motif (**Figure 4A upper panel, and S6A**). Loci
261 containing multiple CTCF-binding motifs display more complex TOP2 CC patterns (**Figure**
262 **4A upper panel, and S6B**) with enrichment on both sides of the double motif, as would be
263 expected from the aggregation of a heterogeneous population of CTCF and TOP2 activity
264 present across different cells.
265
266 We next stratified CTCF motifs into quantiles based on proximal CTCF binding intensity,
267 and aggregated CC-seq signals centred on these loci (**Figure 4A, middle and bottom**
268 **panels**). Most Top2 CC signal is concentrated in two peaks located ±~54 bp relative to the
269 centre of the CTCF motif, with the upstream peak ~2-fold more intense (**Fig 4A, middle**
270 **and bottom panels**). Remaining Top2 CC signal is focused in a flanking array of weaker
271 peaks. This signal pattern has been reported recently for VP16-induced DSBs (Canela et
272 al., 2017; Gothe et al., 2018), and has been suggested to result from a role for TOP2 in
273 facilitating genome organisation by cohesin-dependent loop extrusion operating in the
274 context of CTCF and other boundary elements. In support of this interpretation, total
275 aggregated TOP2 CC signal across these regions is positively correlated with CTCF
276 occupancy as measured by ChIP-seq (**Figure 4A, middle and bottom**); interestingly
277 however, TOP2 CCs were not correlated with interaction strength of associated loops
278 (**Figure S6C**), annotated previously by Hi-C (Darrow et al., 2016). The positions of TOP2 CC
279 surrounding CTCF motifs anticorrelate with the well-positioned nucleosomes at these sites

(**Figure 4B**). However, such anticorrelation with nucleosome positioning is not a unique feature of CTCF loci, but is instead a general property of all TOP2 CC sites (**Figure 4C**), consistent with maps of both Top2 CC (**Figure S3B**) and Spo11 (**Figure S1E;** (Pan et al., 2011)) in *S. cerevisiae*.

In human cells, etoposide-induced TOP2 CCs are also enriched around gene TSSs (**Figure 5**), typically concentrated in broad peaks ~1-2 Kbp downstream and ~0.5-1 Kbp upstream of the TSS (**Figure 5A**; (Yang et al., 2015)). Similar to elsewhere in the genome, in the region immediately downstream of the TSS (0-400 bp), TOP2 CC signal anticorrelated with nucleosome occupancy (**Figure S6D**). Stratifying TSSs based on gene expression microarray data (Ganem et al., 2014) revealed a strong positive correlation between TSS-proximal TOP2 CC enrichment and gene expression (**Figure 5A, middle and bottom**)—something not identified when prior etoposide-induced DSB maps were compared to nascent transcription as measured by GRO-Seq (Canela et al., 2017). Thus, while human TOP2 activity is correlated with total transcription of the gene, it is not proportional to local RNA polymerase activity when assayed at finer scale—suggesting a model where, as postulated for *S. cerevisiae* (**Figure S3A**), superhelical stress is resolved at sites dislocated from the process that generates them. Indeed, when analysed with an identical pipeline, both TSS-proximal TOP2 CCs (**Figure 5A**) and etoposide-induced DSBs (Canela et al., 2017) positively correlate with gene expression (**Figure S6E**), indicating that this correlation is not due to technical differences in mapping methodologies. Based on the twin-domain model of DNA supercoiling, topological stress is expected to increase not just with gene expression level, but also with increasing gene length (Liu and Wang, 1999). In support of this idea, we observe a strong positive correlation between human TOP2 CC enrichment and gene length (**Figure S7A, top**) independent from gene expression (**Figure S7A, bottom**). Interestingly, no such correlation with gene length is present in *S. cerevisiae* (**Figure S7B**), further supporting a model whereby, in this compact gene-dense genome, Top2 activity in the IGR is neither directly linked to expression nor length of the proximal gene.

Notably, the increased density of etoposide-induced human TOP2 CCs at strongly expressed genes is 2.7-fold greater than at strongly bound CTCF motifs (**Figure 5B and C**). Thus, whilst strongly-bound CTCF motifs (14,924) greatly outnumber active genes (4,194)—leading, globally, to more TOP2 activity in total at CTCF sites (**Figure 5D**)—our data reinforce the important role of topoisomerase activity during transcription.

315

316 **Local DNA sequence and methylation status direct the formation of Top2 CCs**

317 Previous reports suggest that etoposide induces a majority of SSBs, rather than DSBs, due
318 to independent poisoning of each active site in the Top2 homodimer (Bromberg et al.,
319 2003). In our yeast and human datasets, we similarly observe more single-strand Top2 CCs
320 (90.1% and 94.2%, respectively) than double-strand Top2 CCs (9.9% and 5.8%,
321 respectively) following etoposide exposure (**Figure 6A**). Interestingly, *MRE11* deletion
322 increased the proportion of double-strand Top2 CCs (**Figure S3C** 12.9%, z-test p-value <
323 2.2×10^{-16}), consistent with the role of MRN/X in protein-linked DNA repair (Neale et al.,
324 2005; Garcia et al., 2011; Anand et al., 2016; Cannavo and Cejka, 2014; Cannavo et al.,
325 2018; Hoa et al., 2016; Hartsuiker et al., 2009).

326

327 Prior, fine-scale mapping of Top2 cleavage at specific substrates indicated that cleavage
328 patterns are influenced by local DNA sequence composition (Pommier et al., 1991;
329 Borgnetto et al., 1996; Strumberg et al., 1999; Wu et al., 2011). To investigate the generality
330 of such findings, and to precisely determine how DNA sequence influences Top2 site
331 preference across the yeast and human genome, we computed the nucleotide resolution
332 average base composition around Top2 CC SSB and DSB sites (**Fig 6B**)—something made
333 possible by the positional accuracy of our mapping technique. For DSBs, average DNA
334 sequence patterns are rotationally symmetrical around the dyad axis of cleavage (**Figure
335 6B, left)**, consistent with the known homodimeric nature of eukaryotic Top2 (Pommier et
336 al., 2016). Base positions with notable skews are restricted to the region ±11 bp from the
337 dyad axis ($p<10^{-4}$, Chi-squared test), consistent with the DNA contacts made by Top2 (Lee
338 et al., 1989; Thomsen et al., 1990; Wu et al., 2011), yet with minor, species-specific
339 differences at a few positions (±2, ±7, ±9; **Figure 6C, top**), suggesting subtle differences in
340 the ScTop2 and HsTOP2 DNA binding surface. Positions -3 and +3 are the bases
341 immediately 5' to the scissile phosphodiester bonds cleaved by Top2 (**Figure 6B**). In the
342 averaged DSB sequence motif, strong preference for cytosine at these positions (69.0% of
343 DSBs) on the scissile strand (**Figure 6B, left)** agrees with *in vitro* studies of Top2
344 mechanism—attributed to favourable base-stacking interactions of etoposide with
345 guanosine at the -1 position on the non-scissile strand (Pommier et al., 1991; Strumberg et
346 al., 1999; Wu et al., 2011).

347

348 Importantly, whilst SSBs display similar overall symmetrical sequence features as DSBs,
349 SSBs differed substantially at position +3, where the strong preference for guanine on the

scissile strand (and paucity of cytosine on the non-scissile strand) is absent (**Figure 6B, right, and Figure 6C, bottom**). Furthermore, the preference for cytosine at the -3 position on the scissile strand increases to 88.1% for SSBs. This clear difference in sequence bias provides strong evidence that such positions truly reflect sites of preferred VP16-induced SSBs vs DSBs *in vivo*.

The human genome is subject to methylation of cytosine (meC) at CpG sites. Dramatically, meC completely abolishes the formation of VP16-induced TOP2 CCs (**Figure 6D**), suggesting this bulky group may interfere sterically with the VP16-Top2-DNA ternary complex, modifying TOP2 catalysis. Collectively, these observations demonstrate that local DNA sequence composition—including epigenetic marks—are major determinants of both TOP2 CC abundance and the differential generation of SSBs and DSBs by VP16 *in vivo*.

Discussion

Topoisomerases are ubiquitous gatekeepers to the genetic material—facilitating changes to DNA topology, nuclear organisation, and chromosome segregation that are essential for the generation and propagation of all life on Earth. Yet, topoisomerase dysfunction can also prove harmful, generating difficult to repair protein-linked DNA breaks that create risks to genome stability. Thus, understanding how, where, and when topoisomerase activity takes place is of great importance. Here, we demonstrate a robust, technically simple and sensitive method to map sites of preferred type IIA topoisomerase activity across the eukaryotic genomes of yeast and human cells at strand-specific nucleotide resolution. Our methodology joins an extensive toolkit of complementary NGS solutions (Canela et al., 2017; Crosetto et al., 2013; Yan et al., 2017), each with its own set of unique advantages. However, many of these techniques do not achieve nucleotide resolution, either due to the use of nucleolytic processing to blunt 5' DNA termini (Canela et al., 2017), and/or inability to directly map DNA breaks covalently linked to protein (Canela et al., 2017; Crosetto et al., 2013; Yan et al., 2017). Here, by utilising the tyrosyl phosphodiesterase activity of recombinant Tdp2 to unblock 5'-DNA termini non-nucleolytically, we are able to accurately map the position of not just Top2 CCs, but also related classes of topoisomerase-like enzymes such as Spo11, which acts uniquely in meiotic cells. Importantly, such specificity in our cleavage maps enable us to corroborate and extend—with completely independent methodology—prior research findings from meiosis (Pan et al., 2011), the impact that VP16 has on SSB versus DSB formation—and for the first time demonstrate the influence that

primary DNA sequence composition and methylation status has on the process of Top2 catalysis *in vivo* in both yeast and human cells.

Top2 activity has long been associated with transcriptional activity (Yang et al., 2015; Brill et al., 1987; Baranello et al., 2014; Yu et al., 2017). In addition, recent research has identified etoposide-induced DSBs that colocalise with a subpopulation of chromatin-bound TOP2 on the loop-external side of CTCF- and Rad21-bound CTCF motifs (Canela et al., 2017; Uusküla-Reimand et al., 2016). TOP2 activity at these sites has been proposed to facilitate genome organisation driven by chromatin loop extrusion, and thereby to constitute a major fraction of the total nuclear TOP2 activity (Canela et al., 2017). Moreover, contrary to expectations, the frequency of etoposide-induced DSBs was found to be locally uncorrelated with nascent RNA levels (Canela et al., 2017)—generating some confusion in the understanding of where TOP2 activity is most prevalent and most important. Here, our independent CC-seq method and analyses permit us to revisit this question in explicit detail, and clarify the role of TOP2 in these processes. Importantly, whilst Top2 activity is certainly highly enriched at CTCF-bound genomic loci, the total amount of activity at any given CTCF locus is many times lower than observed at transcriptionally active genes. Nevertheless, it is critical to emphasise that because of the great abundance of CTCF-bound sites compared to active genes, total aggregated TOP2 activity is globally similar for CTCF-associated versus transcriptionally active regions of the genome.

Our data also permit us to investigate how other genomic features influence Top2 activity. For example, at both TSS and CTCF-proximal regions—and indeed in the wider genome of both yeast and human—Top2 cleavages are highly enriched in nucleosome-free DNA, in support of prior findings made at a subset of genomic loci (Capranico et al., 1990; Udvardy and Schedl, 1991; Käs and Laemmli, 1992). Notably, whilst yeast Top2 activity is also enriched near TSSs, it is concentrated immediately (120-140 bp) upstream, unlike human TOP2 activity, which is primarily concentrated in a broader peak 1-2 kb downstream, within the gene body. Furthermore, unlike human TOP2, yeast Top2 activity is uncorrelated with downstream gene expression. These differences may stem from the very different scale and transcriptional organisation of the yeast and human genomes, and the strong patterning of Top2 activity driven by accessibility to nucleosome-free intergenic promoter regions in *S. cerevisiae*. In support of this interpretation, similar nucleosomal constraints appear to substantially govern the activity of the related topoisomerase-like enzyme, Spo11, during meiosis (Pan et al., 2011) (**Figure S1** herein).

420

421 Despite these differences in distribution of Top2 activity at this larger scale, the DNA
422 sequence preferences for yeast and human Top2 are similar, implying substantial
423 conservation of the DNA binding interface, which is supported by analysis of the published
424 crystal structure of VP16-TOP2-DNA (Wu et al., 2011). A nucleotide resolution genome-
425 wide map of *E. coli* gyrase activity was recently reported (Sutormin et al., 2018)), revealing a
426 sequence motif composed of a central 35 bp region containing the cleavage site, plus two
427 flanking 47 bp regions with ~10.5 bp periodicity centred ~±40 bp from the site of cleavage,
428 which are attributed to the known wrapping of proximal DNA around the gyrase C-terminal
429 domains (Reece and Maxwell, 1991). Strikingly, whilst we observe a core central motif for
430 Top2, there are no such flanking motifs over these ranges, in agreement with its lack of
431 DNA wrapping domains (**Figure S3D**). We do, however, observe two more-proximal
432 flanking regions centred ~±20 bp from the site of cleavage, each with ~10.5 bp periodicity
433 (**Figure S3E**), suggesting that Top2 also bends its DNA substrate—in agreement with a
434 recent biophysical study (Huang et al., 2017).

435

436 We have used CC-seq to probe MRX-dependent repair of Top2 CCs in *S. cerevisiae*,
437 corroborating and extending prior genetic experiments in this organism (Hamilton and
438 Maizels, 2010; Stepanov et al., 2008; Garcia et al., 2011), and others (Nakamura et al.,
439 2010; Hoa et al., 2016; Hartsuiker et al., 2009). Importantly, calibration of our signal using
440 an internal human standard enables the relative quantification of Top2 CCs, and thus
441 directly demonstrates for the first time that loss of Mre11 activity increases cellular levels of
442 Top2 CCs in *S. cerevisiae*. The advantage of the antigen-independent enrichment step is
443 three-fold. Firstly, the spike-in standard contains human TOP2 CCs, which are enriched to
444 a similar extent as the yeast Top2 CCs, and should therefore be less susceptible to
445 variation than background DNA. Secondly, the spike-in standard requires no genetic
446 epitope-tagging or reconstitution of recombinant protein-DNA complexes, unlike ChIP-seq
447 calibration methods (Hu et al., 2015; Grzybowski et al., 2015). Finally, we believe that this
448 calibration step could be performed using any other organism with a suitably divergent
449 genome. Thus, the capacity of CC-seq to quantify as well as map CCs between samples
450 makes this technique ideally suited to the future study of repair dynamics.

451

452 We have demonstrated that CC-seq maps CCs of both human TOP2α and TOP2β—
453 proteins that are conserved amongst all vertebrates and whose functional differences
454 remain a subject of interest within the field (Austin et al., 2018). Given the essential

requirement for TOP2α during mitosis (Akimitsu et al., 2003), and the apparent inability of TOP2β to compensate for its loss (Grue et al., 1998), it will be particularly interesting to determine the genomic distribution of TOP2α/TOP2β activities throughout the cell cycle, and to relate this to 3D chromatin conformation measured by Hi-C. Whilst not essential for cell proliferation, TOP2β plays an important role in promoting transcriptional programmes associated with neuronal development (Tiwari et al., 2012), and this function cannot be supported by TOP2α. Furthermore, loss of TDP2 function inhibits TOP2-dependent gene transcription and leads to neurological symptoms including intellectual disability, seizures and ataxia (Gómez-Herreros et al., 2014). Thus, accurate genomic maps of TOP2β CC formation in these tissues will help to identify those genes most pertinent to the development of neurodegeneration. Moreover, as demonstrated by our Spo11 maps, the antigen-independent, high-efficiency protein-DNA enrichment process makes CC-seq generally applicable for mapping not just Top2 activity in diverse organisms, but also for mapping similar types of topoisomerase-DNA covalent complexes, or even those less distinct DNA-protein crosslinks that arise upon ablation of the DNA-dependent protease SPRTN/Wss1 (Stingele et al., 2015).

Acknowledgements

We thank Keith Caldecott, Antony Oliver and Peter Hornyak for sharing recombinant TDP2, and Jon Nitiss for sharing the *pdr1*Δ strains.

Author Contributions

W.G., D.J. and M.J.N. conceived the project and developed the CC-seq methodology. W.G., D.J., H.T. and R.A. generated whole genome CC-seq libraries. W.G. performed all data processing and analysis, and all human cell work. D.J., H.T. and R.A. performed yeast sensitivity and meiotic DSB assays. T.J.C. developed the mapping pipeline and associated tools. W.G. and M.J.N. interpreted the observations and wrote the manuscript.

Competing interests

The authors declare no competing financial interests.

Funding statement

W.G., D.J., R.A., T.J.C., and M.J.N. were supported by an ERC Consolidator Grant (#311336), the BBSRC (#BB/M010279/1) and the Wellcome Trust (#200843/Z/16/Z).

489

490 ## Data availability

491 All strains and cell lines listed in Table S3 and S4 are available on request. Sequencing
492 reads are available via the NCBI Sequence Read Archive (accession numbers pending).

493

494 ## Methods

495 **Yeast strains, culture methods and treatment**

496 The *Saccharomyces cerevisiae* yeast strains used in this study are described in **Table 2** and
497 were derived using standard genetic techniques. Strains used for Spo11 mapping are
498 isogenic to the SK1 subtype and carry the *sae2*Δ::kanMX gene disruption allele. Strains
499 used for Top2 mapping are isogenic to the BY4741 subtype and carry the *pdr1DBD-CYC8*
500 drug sensitivity cassette (Stepanov et al., 2008). For Spo11 DSB mapping, cells were
501 induced to undergo synchronous meiosis as follows: Cells were grown overnight to
502 saturation in 4 ml YPD medium (1% yeast extract, 2% peptone, 2% glucose supplemented
503 with 0.5 mM adenine and 0.4 mM uracil) at 30 ˚C, then diluted to OD_{600} 0.2 in 200 ml YPA
504 medium (1% yeast extract, 2% peptone, 1% potassium acetate) and grown vigorously for
505 15 h at 30 ˚C. Cells were then washed with water, resuspended in 200 ml sporulation
506 medium (2% potassium acetate supplemented with diluted amino acids), incubated
507 vigorously for 6 h at 30 ˚C and harvested by centrifugation. For etoposide treatment, cells
508 were grown overnight to saturation in 4 ml YPD medium at 30 ˚C, then diluted to OD_{600} 0.5
509 in 100 ml YPD and grown until OD_{600} 2. 50 ml cultures were then incubated for a further 4 h
510 in the presence of either 1 mM etoposide or 2% DMSO, before harvesting by
511 centrifugation.

512

513 **Human cell lines, culture methods and treatment**

514 The human cell lines used in this study are described (**Supplementary Table 3**). Human
515 hTERT RPE-1 cells were obtained from ATCC and cultured at 37 ˚C, 5% CO_2 and 3% O_2 in
516 Dulbecco's Modified Eagle's Medium DMEM/F-12 (Sigma), supplemented with 10% Fetal
517 Calf Serum (FCS) and 90 Units/ml Penicillin-Streptomycin. For all experiments (CC-seq,
518 Slot Blot, WB, IF, FACs) with asynchronous cell populations, RPE-1 cells were seeded at a
519 density of ($3.5x10^3$ cells/cm^2l) and incubated for 72 h at 37 ˚C, to ensure subconfluent log-
520 phase growth (~70% confluency) at the time of the experiment. For G1 cell populations, WT
521 and *TOP2B*$^{-/-}$ RPE-1 cells were seeded at a density of $5x10^3$ cells/cm^2 and incubated for 48
522 h at 37 ˚C in DMEM/F12 containing 10% FCS, prior to a further 24 h incubation in

523 DMEM/F12 medium containing no FCS to ensure complete G1-phase arrest (verified by
524 FACs, see below). For experiments with proteasome inhibitor and etoposide (CC-seq, Slot
525 Blot), cells were preincubated with 5 μM MG132 (Sigma) for 90 min, trypsinised and
526 incubated in suspension with 5 μM MG132 and 100 μM etoposide (Sigma) for 20 min at 37
527 ˚C. For experiments with etoposide alone (IF), adherent cells were treated with 100 μM
528 etoposide for 20 min at 37 ˚C.
529

530 **Generation of *TOP2B*$^{-/-}$ RPE-1 cells**

531 The oligonucleotides 5'-CACCGCCGCAGCCACCCGACT and 5'-
532 AAACAGTCGGGTGGCTGCGGC (identified using Benchling; https://benchling.com) were
533 annealed and cloned into pX330 following BbsI restriction, as described previously (Hsu et
534 al., 2013). This SpCas9/ trugRNA co-expression plasmid was transiently expressed in RPE-
535 1 cells to target the 17 bp target sequence GCCGCAGCCACCCGACT (TGG) within exon 1
536 of *TOP2B*. Single clones were trypsinised and passaged to isolated culture vessels prior to
537 screening for absent protein by Western Blot (WB). All experiments involving *TOP2B*$^{-/-}$ were
538 conducted using the RPE-1 clone T2B/6, in which no TOP2β is detectable by WB or IF.
539

540 **Spot tests of chronic etoposide sensitivity**

541 Single colonies of each *S. cerevisiae* strain were incubated overnight in 4 ml YPD at 30 ˚C
542 with shaking. 0.1 ml of this starter was used to inoculate 4 ml YPD, prior to incubation for 5
543 hours at 30 ˚C. Cultures were diluted to make a stock with an OD_{600} of 2.0, then this was
544 10-fold serially diluted five times. Each dilution was spotted onto plates containing 0, 0.1,
545 0.3 or 1.0 mM VP16, prior to incubation for three days at 30 ˚C. Plates were imaged on a
546 2400 Photo scanner (Epson).
547

548 **Southern blotting of meiotic Spo11 DSBs**

549 Approximately 2 μg of genomic DNA (isolated by non-proteolysing Phenol-Chloroform
550 extraction, as described below) was digested at 37 °C overnight using *Pst*I restriction
551 enzyme (NEB) in NEBuffer 3.1 (100 mM NaCl, 50 mM Tris Base·HCl pH 7.9, 10 mM $MgCl_2$,
552 100 μg ml-1 BSA). Additional *Pst*I was added for 4 hours before the addition of NEB purple
553 loading dye to 1×. Digested samples were proteolysed using 1 mg ml-1 Proteinase K
554 (Sigma) at 60 ˚C for 30 minutes, left to reach room temperature before 10 μg was loaded on
555 a 0.7% 1× TAE agarose gel (40 mM Tris Base·HCl, 20 mM glacial acetic acid, 1 mM EDTA
556 pH 8.0) containing 50 μg ml-1 ethidium bromide. DNA was separated in 1× TAE at 60 V for
557 18 hours. The gel was imaged using InGenius (Syngene) bioimaging system to check

558 migration and then exposed to 180 mJ/m^2 UV in the Stratalinker (Stratagene). The gel was
559 then soaked in three times its volume of denaturation solution (0.5 M NaOH, 1.5 M NaCl) for
560 30 minutes and then transferred to Zetaprobe (Bio-Rad) membrane by means of a vacuum
561 at 55 mBar for 2 hours. After transfer the membrane was washed in water ten times and
562 then cross-linked by exposing the membrane to 120 mJ/m^2 UV in the Stratalinker. The
563 membrane was incubated in 30 ml of hybridisation buffer (0.5 M $NaHPO_4$ buffer pH 7.5, 7%
564 SDS, 1 mM EDTA, 1% BSA) at 65 ˚C for 1 hour. The *MXR2* probe for looking at the
565 *HIS4::LEU2* locus was created from 50 ng of template DNA, 0.1 ng of Lambda DNA (NEB)
566 digested with *BstE*II (NEB), and water. The mix was denatured at 100 °C for 5 minutes then
567 put on ice. High Prime (Roche) was added in addition to 0.5-3 mBq of α-^{32}P dCTP and
568 incubated at 37 °C for 15 minutes. 30 µl 1× TE was added and the probe spun through a G-
569 50 spin column (GE Healthcare) at 400 × *g* for 2 minutes. The probe was then denatured by
570 incubating at 100 °C for 5 minutes and then put on ice before being added to 20 ml
571 hybridisation mixture. The original 30 ml hybridisation buffer was discarded and the 20 ml
572 containing the probe was added to the membrane and incubated overnight at 65 ˚C. After
573 incubation, the membrane was washed five times with 100 ml pre-warmed Southern wash
574 buffer (1% SDS, 40 mM $NaHPO_4$ buffer pH 7.5, 1 mM EDTA) and exposed to phosphor
575 screen overnight.
576

577 **Western blotting**

578 Whole human cell extracts (WCE) were harvested by direct lysis in 1x Laemmli loading
579 buffer, denatured for 10 min at 95 ˚C and sonicated for 30 s using Bioruptor® Pico.
580 Samples were subjected to SDS-PAGE (7% or gradient gel) and transferred to
581 nitrocellulose membrane. Primary immunodetection was with antibodies targeting TOP2β
582 (Clone 40, BD Biosciences), TOP2α (ab52934, Abcam), or Ku80 (ab80592, Abcam).
583 Secondary immunodetection was with HRP-conjugated Rabbit anti-Mouse IgG
584 (ThermoFisher), prior to detection of peroxidase activity using ECL reagent and X-Ray film
585 (Scientific Laboratory Supplies Ltd).
586

587 **Slot blotting**

588 Samples were diluted 4-fold (500 uL total volume) in $NaPO_4$ buffer (25 mM, pH 6.5), and slot
589 blotted onto 0.2 µM nitrocellulose membrane (Amersham), using the Minifold I (Whatman)
590 manifold. The wells were washed twice with 750 µL $NaPO_4$ buffer. The membrane was then
591 blocked with 10% milk-TBST for 1 h at RT, prior to incubation overnight with anti-TOP2β
592 antibody (Clone 40, BD Biosciences) at 4 ˚C. The membrane was washed 4 times with

593 TBST, incubated with HRP-conjugated Rabbit anti-Mouse IgG (ThermoFisher) for 1 h at RT,
594 washed 4 times with TBST, and incubated with ECL detection reagent for 1 min. X-Ray film
595 was used for detection.
596
597 **Fluorescence-Assisted Cell Sorting (FACS)**
598 Approximately 10 million RPE-1 cells were trypsinised, washed once in PBS and
599 resuspended in 1.5 ml PBS. 3.5 ml ethanol was added dropwise to pellet, with vortexing.
600 Cells were fixed for 1 hr at 4 ˚C, prior to centrifugation and aspiration of the supernatant.
601 Cells were washed twice with PBS, prior to resuspension in 0.5 ml 0.25% Triton-X100-PBS
602 for 15 min on ice. Cells were pelleted by centrifugation, supernatant was aspirated, and the
603 pellet was resuspended in 0.5 ml TBS containing 10 ug/ml RNase A (Sigma) and 167 nM
604 Sytox Green (ThermoFisher). After 30 min incubation in the dark at RT, the suspension was
605 filtered through fine mesh into test tubes. DNA content in 50,000 cells was analysed using
606 the Accuri C6 (BD Biosciences), with gating to exclude doublets and cell debris.
607
608 **Immunofluorescence**
609 Cells were seeded onto glass coverslips (Agar Scientific), incubated and treated according
610 to the protocol outlined above. Cells were then fixed with 4% paraformaldehyde PBS for 10
611 min, washed three times with PBS, permeabilised with 0.2% Triton-X100-PBS for 10 min,
612 blocked for 1 h with 10% FCS-PBS, incubated with primary antibodies targeting Phospho-
613 Histone H2AX (S139) (JBW-301, Merck Millipore) and TOP2α (ab52934, Abcam), washed
614 three times with PBS, incubated with secondary antibodies Alexa 488-conjugated Goat
615 anti-mouse IgG (Fisher) and Alexa 647-conjugated Goat anti-Rabbit (Fisher), washed three
616 times with PBS, washed once with distilled water, and mounted with VECTASHIELD
617 containing DAPI (Vector Laboratories).
618
619 **High-content microscopy**
620 Automated wide-field microscopy was performed on an Olympus ScanR system (motorised
621 IX83 microscope) with ScanR Image Acquisition and Analysis Software, 40x/0.6
622 (LUCPLFLN 40x PH) dry objectives and Hamamatsu ORCA-R2 digital CCD camera
623 C10600. Numbers of anti-phospho-Histone H2AX (S139) foci (Alexa 488; FITC filter) were
624 quantified in the nuclear region colocalising with DAPI, using Olympus ScanR Analysis
625 software. TOP2α signal (Alexa 647; Cy5 filter) was also quantified in this region.
626 **CC-seq: Enrichment of protein-linked DNA**

627 $1.5x10^7$ RPE-1 cells were treated as described above, pelleted by centrifugation, washed
628 once with 15 ml ice-cold PBS, and resuspended in three aliquots of 400 µL ice-cold PBS.
629 $1x10^9$ yeast cells were treated as described above, then spheroplasted in 1.5 ml
630 spheroplasting buffer (1 M sorbitol, 50 mM $NaHPO_4$ buffer pH 7.2, 10 mM EDTA) containing
631 200 µg/ml Zymolyase 100T (AMS Biotech) and 1% β-mercaptoethanol (Sigma) for 20 min at
632 37 ˚C. 2 µL Protease Inhibitor Cocktail and 2 µL Pefabloc (Sigma) were added before
633 splitting into five aliquots of 400 µL. All subsequent steps of the protocol are the same for
634 yeast and human samples. 1 ml ice-cold ethanol was added to 400 µL cell suspensions in
635 microcentrifuge tubes, mixed, incubated for 10 min on ice, and pelleted by centrifugation.
636 Supernatant was thoroughly removed by aspiration, prior to addition of 200 µL 1x STE
637 buffer (2% SDS, 0.5M Tris pH 8.1, 10 mM EDTA, 0.05% bromophenol blue), cell disruption
638 using a pestle (VWR), addition of a further 400 µL 1x STE buffer, and incubation for 10 min
639 at 65 ˚C. Samples were cooled on ice and 500 µL Phenol-Chloroform-isoamyl alcohol
640 (25:24:1; Sigma) added. Mixtures were emulsified by shaking and pipetting 5 times with a 1
641 ml micropipette, prior to phase separation by centrifugation at 20,000 g for 20 min. By
642 minimising mechanical shearing of the lysate prior to phenol chloroform extraction,
643 peptides that are covalently linked to high molecular weight DNA partition into the aqueous
644 phase. 500 µL of the aqueous phase was removed to a clean microcentrifuge tube and
645 nucleic acids precipitated with 1 ml ice-cold ethanol, pelleted by centrifugation, washed
646 with ice-cold 70% ethanol, and dissolved in TE buffer overnight at 4 ˚C. Samples were then
647 incubated with 0.2 mg/ml RNase A (Sigma) for 1 h at 37 ˚C; nucleic acids were precipitated
648 with 1 ml ethanol, pelleted by centrifugation, washed twice with 70% ethanol and dissolved
649 in TE overnight. Aliquots were combined to a total of 1 ml and sonicated to an average
650 fragment size of 300-400 bp with Covaris (duty cycle: 10%, intensity/peak power incidence:
651 75W, cycles/burst: 200, time: 15 min). 1 ml of sonicated sample was added to 1.2 ml of
652 binding buffer (10 mM Tris pH 8.1, 10 mM EDTA, 0.66 M NaCl, 0.22% SDS, 0.44% N-
653 Lauroylsarcosine sodium salt). Each sample was divided over several Miniprep (QIAGEN)
654 silica-fibre membrane spin columns, such that the total DNA loaded to each was
655 approximately 20 µg. The flowthrough was reapplied to the column to improve binding.
656 Columns were washed 6 times with 600 µL of TEN (10 mM Tris, 1 mM EDTA, 0.3 M NaCl)
657 per 1 min wash, prior to elution with 100 µL TES (10 mM Tris, 1 mM EDTA, 0.5% SDS).
658

659 **CC-seq: DNA end repair and adapter ligation**

660 Eluted products were pooled to 500 µL in TES and incubated with 1 mg/ml Proteinase K
661 (Sigma) for 30 min at 60 ˚C, prior to overnight ethanol precipitation at -80 ˚C with 1.41 ml

662 ethanol, 0.2 mg/ml glycogen and 200 mM NaOAc. The DNA-glycogen precipitate was
663 pelleted by centrifugation at 20,000 g for 1 hr at 4 ˚C, washed once with 1.5 ml 70%
664 ethanol, and re-pelleted by centrifugation. The supernatant was aspirated and the pellet
665 was air-dried for 10 min at RT, prior to solubilisation in 52 µL 10 mM Tris-HCl. DNA
666 concentration was measured in a 2 µL sample with the Qubit (ThermoFisher) and High
667 Sensitivity reagents. The remaining 50 µL was used as input for one round of end repair
668 and adapter ligation with NEBNext Ultra II DNA Library Preparation kit (NEB), according to
669 manufacturer's instructions, except for the use of a custom P7 adapter (see table). The use
670 of custom adapters is to allow differentiation of the sheared end (P7 adapter) from the
671 Top2/Spo11 end (P5 adapter). After ligation of the P7 adapter, DNA was isolated with
672 AMPure XP beads (Beckman Coulter) according to manufacturer's instructions (beads:input
673 of 78:90) and eluted in 50 µL 10 mM Tris-HCl. Samples were diluted 2-fold with 50 µL Tdp2
674 reaction buffer (100 mM TrisOAc, 100 mM NaOAc, 2 mM MgOAc, 2 mM DTT, 200 µg/ml
675 BSA) and incubated with 3 µL of 10 µM recombinant human TDP2 (Hornyak et al., 2016;
676 Johnson et al., 2019), for 1 h at 37 ˚C. DNA was isolated again with AMPure XP beads
677 (beads:input of 103:103) and eluted in 52 µL 10 mM Tris-HCl. Next, a second round of end
678 repair and adapter ligation was conducted, using adapter P5 (see table). After ligation of
679 the P5 adapter to the Top2/Spo11-cleaved end, DNA was isolated with AMPure XP beads
680 (beads:input of 78:90) and eluted in 17 µL 10 mM Tris-HCl.
681

682 **CC-seq: PCR and size selection**

683 DNA concentration was measured in 2 µL using the Qubit. The remaining 15 µL was used
684 as template for the PCR step of the NEBNext Ultra II PCR step using universal primer (P5
685 end) and indexed primers for multiplexing (P7 end), according to manufacturer's
686 instructions. PCR reactions were diluted with 50 µL 10 mM Tris-HCl, DNA was isolated with
687 AMPure XP beads (beads:input of 84:100) and eluted in 30 µL 1 mM Tris-HCl pH 8.1.
688 Samples were then subjected to 200-600 bp size selection using the BluePippin (Sage
689 Science), prior to quantification of molarity using the Bioanalyzer (Agilent).
690

691 **CC-seq: NGS and data pipeline**

692 Multiplexed library pools were sequenced on the Illumina MiSeq (Kit v3 - 150 cycles) or
693 Illumina NextSeq 500 (Kit v2 - 75 cycles), with paired-end read lengths of 75 or 42 bp,
694 respectively. Paired end reads that passed filter were aligned using bowtie2 (options: -X
695 1000 --no-discordant --very-sensitive --mp 5,1 --np 0), using MAPQ0 settings for yeast or
696 MAPQ10 settings for human experiments, then SAM files processed by the custom-built

697 Perl program termMapper that computes the coordinates of the protein-linked 5'-terminal
698 nucleotide. The reference genomes used in this study are hg19 (human), and Cer3H4L2 (*S.*
699 *cerevisiae*), which we generated by inclusion of the *his4*::*LEU2* and *leu2*::*hisG* loci into the
700 Cer3 yeast genome build. Yeast data sets were filtered to exclude long terminal repeats,
701 retrotransposons, telomeres, and the rDNA. Human datasets were filtered to remove known
702 ultra-high signal regions (Hoffman et al., 2013; ENCODE, 2012) and repeat regions
703 (ENCODE, 2012). All subsequent analyses were performed in R (Version 3.4.3) using
704 RStudio (Version 1.1.383), unless indicated otherwise.
705

706 **CC-seq: Calibrated library generation**

707 Calibration of Top2 CC-seq experiments was conducted to allow comparison of relative
708 peak intensities in different yeast strains. This was achieved by spike-in of human DNA
709 following the sonication stage of the protocol, which is a method that has been used to
710 calibrate other sequencing methods (Hu et al., 2015; Grzybowski et al., 2015). S. cerevisiae
711 and RPE-1 cells were exposed to etoposide and processed until just after sonication,
712 exactly as according to the cell treatment and CC-seq protocols above. DNA concentration
713 was quantified by Qubit, and then mixed at a molar ratio of human DNA:yeast DNA of
714 1:100. All subsequent stages of the protocol were identical, except read alignment, for
715 which we used both hg19 and Cer3H4L2 builds successively. Cer3H4L2-aligned peak
716 heights were corrected in each sample by multiplying by the reciprocal fraction of human
717 reads in that sample.
718

719 **CC-seq: Fine-scale mapping**

720 Fine-scale (nucleotide resolution) maps of Spo11/Top2 CCs were produced as simple
721 histograms over a specified region (**Figures 1B, 2B, 3D, 4A, 5A, S1A, S3A, S5A and S5B**).
722 Dark red and blue line heights indicate numbers of 5'-terminal nucleotides detected at that
723 position on the Watson and Crick strands, in units of HpM. Where indicated in the figure
724 caption, smoothed data are also plotted as pale red and blue polygons, in addition to the
725 unsmoothed nucleotide resolution data. This smoothing was either applied using a sliding
726 Hann window of the indicated width, or using a custom smoothing function (VarX), as
727 indicated in the figure caption.
728

729 **CC-seq: Broad-scale mapping**

730 Broad-scale maps of Top2 CCs were produced by binning nucleotide resolution data at 10
731 Kbp (**Figure 3B**) or 100 Kbp (**Figure S4D**) resolution. Binned data were either plotted

directly (Figure S4D); or first scaled according to the estimated noise fraction (see below), smoothed with a 10-bin Hanning window, and median subtracted (Figure 3B).

CC-seq: Estimation of the noise fraction in Human datasets

The noise fraction in each sample was estimated using an adaptation of the previously published NCIS method (Liang and Keleş, 2012). Briefly: the data for -VP16 and +VP16 samples were first binned at 10 Kbp resolution. Then the subpopulation of bins with the lowest TOP2 CC signal was identified in each sample. The average signal density of this subpopulation of bins, in each sample, was defined as the noise density (d_{-VP16} and d_{+VP16}). Signal in the -VP16 sample was scaled by a normalisation factor equal to:

$$r = \frac{d_{+VP16}}{d_{-VP16}}$$

CC-seq: Quantification of Spo11 and Top2 activity in defined genomic regions

Yeast Spo11 hotspots were the same as defined previously (Pan et al., 2011). Yeast intra/intergenomic regions were defined based on TSS and TTS coordinates reported on the Saccharomyces Genome Database (https://www.yeastgenome.org). Human chromatin compartments A and B were defined based on eigenvector analysis of previously published 100 kb resolution RPE-1 Hi-C data (Darrow et al., 2016) using the Juicer package (Lieberman-Aiden et al., 2009; Durand et al., 2016). Human “CTCF” and “TSS” regions were defined as 10 kb regions centred on the top quartile of expressed TSSs or the midpoint of top quartile CTCF-bound CTCF-binding motifs, with overlaps merged using GenomicFeatures::reduce. The “Both” region was defined as the intersection of the “TSS” and “CTCF” regions using GenomicFeatures::intersect. This region was then excluded from the individual “TSS” and “CTCF” regions. The “Neither” region was defined as regions of hg19 which overlapped neither “TSS”, nor “CTCF”, nor “Both”, using GenomicFeatures::gaps. Nucleotide resolution data was tallied within defined regions, and is expressed as an aggregate (bar plots) in which the signal is corrected using the average signal in the “Neither” compartment, and/or as the distribution of region signal densities (box-and-whisker plot), as indicated in figure captions.

CC-seq: Correlation of Watson/Crick cleavage positions

Nucleotide resolution human TOP2 data was thresholded at 0.01 HpM. Nucleotide resolution yeast Top2 and Spo11 data were not thresholded. Peak coordinates on the Crick

strand were offset over the range -100 to +100, relative to Watson coordinates. After each offset, the data was filtered to include only sites with both Watson and Crick hits. The Pearson correlation (*r*) between the Watson and Crick signal intensities in these *n* sites was calculated. We also counted the fraction of reads found within these *n* sites, and normalised this number over the -100 to +100 bp range. Data are expressed as R values and/or normHpM values, as indicated in the figure captions.

CC-seq: Aggregation of CC-seq data around loci of interest

Nucleotide resolution CC-seq data (line-plots) or binned CC-seq data (heatmaps) were aggregated within regions of specified size, centred on the loci of interest. The resulting sum total HpM was divided by numbers of loci to give a mean HpM per locus.

CC-seq: Loci of interest used in this study

Yeast TSS and TTS coordinates were obtained from the Saccharomyces Genome Database https://www.yeastgenome.org. These were stratified based on associated gene length, expression level in vegetative SK1 (GSM907178, GSM907179, GSM907180), or expression level in meiotic SK1 (GSM907176, GSM907177; (Dominissini et al., 2012)). Human TSS and TTS coordinates were obtained from the UCSC hg19 knownGene annotation, and stratified based on associated gene length, or expression level (GSM1395252, GSM1395253, GSM1395254; (Ganem et al., 2014)). Occupied RPE-1 CTCF motifs were identified as follows: The FIMO tool (Grant et al., 2011) and the CTCF Position Weight Matrix (PWM) from the JASPAR database (Mathelier et al., 2014) were used to find all significant hg19 CTCF motifs ($p < 1x10^{-4}$). These were filtered to include only those which overlapped positions of RPE-1 CTCF ChIP-seq peaks (GSM749673, GSM1022665; (ENCODE, 2012)), and stratified based on this ChIP-seq data. RPE-1 loop anchor-associated CTCF motifs were identified using the Juicer MotifFinder (Durand et al., 2016) with the RPE-1 WT Hi-C looplist (GSE71831(Darrow et al., 2016)) and CTCF ChIP-seq BED file (GSM749673, GSM1022665; (ENCODE, 2012)) as input. Human TOP2 CC-seq peak coordinates were identified by thresholding (0.05 HpM) of pooled +VP16 data presented.

CC-seq: Spatial correlation of yeast Top2 and Spo11 signals

Nucleotide resolution Top2/Spo11 CC-seq data was binned at 50 bp resolution and the Pearson correlation was calculated between the sum HpM for all bins at a given inter-bin distance.

800 **CC-seq: Quantifying single and double-strand Top2 CCs**

801 Nucleotide resolution Human and Yeast Top2 CC-seq data were first thresholded at 0.05
802 and 1 HpM, respectively. SSB sites were defined as those sites without a cognate on the
803 opposite strand at the expected offset of 3 bp. DSBs were defined as cognate sites with a
804 3 bp offset. SSB and DSB percentages are expressed as a percentage of the total number
805 of sites (SSB + DSB). A randomisation experiment was conducted in order to estimate
806 expected numbers of SSBs and DSBs within the sample under a random model where
807 signal is distributed independently on each strand. To achieve this, the amplitudes of Top2
808 CCs (HpM) were shuffled amongst the positions in the nucleotide resolution datasets, prior
809 to thresholding and offset analysis as described above.

810

811 **CC-seq: DNA sequence composition of single and double-strand Top2 CCs**

812 Nucleotide resolution Human and Yeast Top2 CC-seq data were first thresholded at 0.05
813 and 1 HpM, respectively. The high frequency positions remaining were classified as part of
814 a single or double-stranded Top2 CC based on absence or presence of a cognate cleavage
815 at the expected W-C offset of 3 bp. For double-stranded Top2 CCs, a dyad axis coordinate
816 was defined as the centrepoint between the Top2-linked nucleotides on the W and C strand
817 (that is, the midpoint of the central two base pairs in the four base pair overhang). For
818 single-stranded Top2 CCs, we used an imaginary dyad axis in the same relative position.
819 DNA sequence was aggregated ±20 bp around these two classes of Top2 CCs. Statistical
820 significance was determined using the one sample (goodness-of-fit) Chi-squared test, as
821 described previously (Pommier et al., 1991).

822

823 **CC-seq - MethylC Analysis**

824 A publically-available RPE-1 reduced representation bisulphite sequencing (RRBS) dataset
825 (two replicates) was used to define coordinates of nucleotides immediately 3'-relative to
826 919,817 unmethylated or 341,136 methylated Cs, based on <10% or >90% methylation.
827 Next we aggregated RPE-1 CC-seq (0.01 HpM thresholded) hits on these loci, and divided
828 by the number of loci to give a density (barplot). Statistical significance was determined by
829 the Kolmogorov-Smirnov test.

830

831 **Ideograms**

832 Human chromosome ideograms were adapted from the open source ideogram package
833 (https://eweitz.github.io/ideogram/).

834

Figure Legends

Figure 1. CC-seq maps covalent Spo11-linked DNA breaks in *S. cerevisiae* meiosis with nucleotide accuracy

A) Schematic of the CC-seq method.

B) Column-based enrichment of Spo11-linked DNA fragments detected by Southern blotting at the *his4*::*LEU2* recombination hotspot (**Methods**). Arrows indicate expected sizes of Spo11-DSBs.

C) Nucleotide resolution mapping of *S. cerevisiae* Spo11 hotspots by CC-seq or oligo-seq (Pan et al., 2011). Red and blue traces indicate Spo11-linked 5' DNA termini on the Watson and Crick strands, respectively. Grey arrows indicate positions of gene open reading frames.

D) Pearson correlation (r) of Spo11 CC-seq signal between Watson and Crick strands, offset by the indicated distances.

E) Average nucleotide composition over a 200 (top) and 30 bp (bottom) window centred on Spo11 breaks. Bases reported are for the top strand only.

HpM = Hits per million mapped reads per base pair.

Figure 2. CC-seq maps covalent Top2-linked DNA breaks in *S. cerevisiae* cycling cells with nucleotide accuracy

A) Serial dilution spot tests of VP16 tolerance for the indicated strains.

B) Nucleotide resolution mapping of *S. cerevisiae* Top2 CCs by CC-seq of the indicated strains after treatment for 4 hours with 1 mM VP16. Spo11-CC data is plotted for comparison. Top2 CC data were calibrated using a human DNA spike-in (**Methods**). Red and blue traces indicate CC-linked 5' DNA termini on the Watson and Crick strands, respectively. Grey arrows indicate positions of gene open reading frames. Lower panels show an expanded view of the region from 31.5 to 40 Kbp.

C) Quantification of Top2 and Spo11 CC signal stratified by genomic region. The genome was divided into intra and intergenic regions; the intergenic region was further divided into divergent, tandem and convergent based on orientation of flanking genes. Spo11 and Top2 activity mapped by CC-seq is expressed as box-and-whisker plots of density (upper and lower box limit: 3rd and 1st quartile; bar: median; upper and lower whisker: highest and lowest values within 1.5-fold of the interquartile range), or as the percentage of total mapped reads.

D) Local correlation of Top2 or Spo11 CC-seq signals. Top2 or Spo11 CC-seq data were binned at 50 bp resolution and the Pearson correlation calculated between bins of increasing separation.

E) Pearson correlation (r) of Top2 CC-seq signal on Watson and Crick strands, offset by the indicated distance.

HpM = Hits per million mapped reads per base pair.

Figure 3. CC-seq maps TOP2-linked DNA breaks in Human cells with nucleotide accuracy

A) Anti-TOP2β western slot blot of input, flow through, wash, and elution fractions. RPE-1 cells were treated or not with VP16, prior to processing according to **Figure 1A**.

B) Broad-scale maps of *H. sapiens* TOP2 CCs produced by CC-seq in RPE-1 cells ±VP16. Raw data were scaled, binned, smoothed and median subtracted prior to plotting (**Methods**). Chromatin compartments revealed by Hi-C eigenvector analysis (Darrow et al., 2016), and supercoiling revealed by bTMP ChIP-seq (Naughton et al., 2013) are shown for comparison.

C) Quantification of TOP2 CC in chromatin compartments A and B. Data are expressed as box-and-whisker plots of density as for **Figure 2C**.

D) Fine-scale mapping of *H. sapiens* TOP2 CCs by CC-seq in RPE-1 cells ±VP16. Red and blue traces indicate TOP2-linked 5' DNA termini on the Watson and Crick strands, respectively. Pale shaded areas are the same data smoothed according to local density (see **Methods**). RPE-1 CTCF and H3K4Me3 ChIP-seq data plus H3K27Ac ChIP-seq data overlaid from seven cell lines (ENCODE, 2012) is shown for comparison.

E) Medium-scale aggregate of END-seq mapped DSBs (Canela et al., 2017) surrounding nucleotide resolution CC-seq mapped TOP2 CCs.
F) Fine-scale strand-specific aggregate of END-seq mapped DSB ends (red and blue bars) and nucleotide resolution CC-seq mapped TOP2 CCs (grey bars) surrounding strong TOP2 CC sites.

Figure 4. CTCF-proximal TOP2 activity is tightly confined within nucleosome-depleted regions
A) Aggregation of TOP2 CCs in a 1 Kbp window centred on orientated CTCF motifs in human RPE-1 cells. Four example CTCF loci are shown orientated in the 5'-3' direction (top). A heatmap of all CTCF-motifs in the human genome, with 25 rows stratified by the strength of colocalising CTCF ChIP-seq peaks in RPE-1 cells (middle). The colour scale indicates average TOP2 CC density. Motifs are also stratified into 4 quartiles of CTCF-binding, and the average TOP2 CC distribution in each quartile plotted (bottom).
B) Aggregated TOP2 CC distribution (red line) in the highest quartile of CTCF-binding compared with the average MNase-seq signal (blue line).
C) Aggregated TOP2 CC distribution (black and red lines: single-nucleotide resolution and smoothed, respectively) and the average MNase-seq signal (blue line) surrounding strong TOP2 CC sites.
In (B) and (C) peaks in MNase-seq signal indicate inferred nucleosome positions (blue circles).

Figure 5. TSS-proximal TOP2 activity is strongly correlated with gene transcription
A) Aggregation of TOP2 CCs in a 10 Kbp window centred on orientated TSSs in human RPE-1 cells. Four example TSSs are shown orientated in the 5'-3' direction (top). A heatmap of all TSSs in the human genome, with 25 rows stratified by gene expression level in RPE-1 cells (middle). The colour scale indicates average TOP2 CC density. Motifs are also stratified into 4 quartiles of gene expression, and the average TOP2 CC distribution in each quartile plotted (bottom).
B) Comparison of CTCF-proximal and TSS-proximal TOP2 CC distributions in the highest quartile of CTCF-binding (pink) and gene-expression (blue), respectively.
C) Average TOP2 CC density in 10 Kbp regions centred on the highest quartile of TSS, CTCF, or regions where both features are present. Data are expressed as box-and-whisker plots of density as in **Figure 2C**. Statistical significance was determined using the KS test.
D) As in (C) but sum total TOP2 CCs found in these regions.

Figure 6. Local DNA sequence and methylation status direct the formation of Top2 CCs
A) The percentage of strong sites that are SSBs and DSBs in etoposide-treated *S. cerevisiae* and human cells.
B) Average nucleotide composition over a 30 bp window centred on the DSB or (inferred) SSB dyad axis, in etoposide-treated *S. cerevisiae* and human cells. Values reported are for the top strand only.
C) Heatmaps describing pairwise similarity of nucleotide composition patterns shown in (B). Rows 1-4 are the absolute differences between: yeast and human SSB patterns, yeast and human DSB patterns, yeast SSB and DSB patterns, and human SSB and DSB patterns, respectively.
D) The average number of TOP2 CCs at the +1 position relative to methylated and unmethylated cytosines in human RPE-1 cells, ±VP16. Statistical significance was determined using KS test.

Supplementary Figure Legends

Figure S1. CC-seq maps covalent Spo11-linked DNA breaks in *S. cerevisiae* meiosis with nucleotide accuracy (related to Figure 1)

A) Correlation of hotspot signals from CC-seq and oligo-seq.

B) Correlation of 500 bp binned Spo11 maps from two representative replicates.

C) Correlation of Spo11 cleavages on Watson and Crick strand when offset by 1 bp (boxed), relative to other offsets from -4 to +4 bp.

D) Spo11 breaks mapped by CC-seq (raw=black, or smoothed=red) anticorrelate with nucleosome occupancy measured by MNase-seq (blue).

E) Aggregation of Spo11 activity in a 10 Kbp window centred on orientated TSSs in *S. cerevisiae*. Three example TSSs are shown orientated in the 5'-3' direction (top). A heatmap of all TSSs in the *S. cerevisiae* genome, with 25 rows stratified by gene expression level in SK1 cells (middle). The colour scale indicates average Spo11 break density. Motifs are also stratified into 4 quartiles of gene expression in meiotic SK1 cells, and the average distribution of Spo11 activity in each quartile plotted (bottom).

Figure S2. CC-seq maps covalent Top2-linked DNA breaks in *S. cerevisiae* cycling cells with nucleotide accuracy (related to Figure 2).

A-C) Correlation of 1 Kbp binned Top2 CC maps from *pdr1*Δ (A), *pdr1*Δ*sae2*Δ (B) and *pdr1*Δ*mre11*Δ (C) cells treated with VP16.

D) Pairwise Pearson correlation values for 100 bp binned Top2 CC maps from all assayed conditions. Each condition is a pool of two biological replicates.

E) Nucleotide-resolution *S. cerevisiae* Top2 CC map of chromosome 3 for all assayed conditions. Each condition is a pool of two biological replicates.

F-H) The normalised number of Top2 CCs retained in the *pdr1*Δ (F), *pdr1*Δ*sae2*Δ (G) and *pdr1*Δ*mre11*Δ (H) cells treated ±VP16, after filtering to include only sites offset by the given number of base pairs. All data were normalised over a -100 to +100 bp window.

I-K) Pearson correlation (r) of Top2 CC-seq signal on Watson and Crick strands, offset by the indicated distance in *pdr1*Δ (I), *pdr1*Δ*sae2*Δ (J) and *pdr1*Δ*mre11*Δ (K) cells treated ±VP16.

Figure S3. Top2-linked DNA breaks in *S. cerevisiae* are not correlated with gene expression, anticorrelate with nucleosomes, and have biased nucleotide skews indicative of bent DNA (related to Figure 2)

A) Top2 CC mapped by CC-seq (raw=black, or smoothed=red) anticorrelate with nucleosome occupancy measured by MNase-seq (blue).

B) Aggregation of Top2 CCs in a 10 Kbp window centred on orientated transcription start sites (TSS) in *pdr1*Δ *S. cerevisiae*. Four example TSSs are shown orientated in the 5'-3' direction (top). Heatmap of all TSSs in the *S. cerevisiae* genome, with 25 rows stratified by gene expression level in vegetative growth (middle). Colour scale indicates average Top2 CC density. Motifs are also stratified into four quartiles of gene expression, and the average distribution of Top2 CCs in each quartile plotted for untreated and +VP16 conditions (bottom).

C) The percentage of strong sites that are SSBs and DSBs in etoposide-treated *pdr1*Δ and *pdr1*Δ*mre11*Δ *S. cerevisiae*. Sites were thresholded at 1 HpM prior to sorting into DSB or SSB classes based on presence or absence of a 3 bp offset cognate (Obs.). As a control, the amplitudes of Top2 CCs (HpM) were randomised amongst the positions in the nucleotide resolution datasets, prior to thresholding and offset analysis as described above (Rand.)

D) Average nucleotide composition over a 200 bp window centred on the DSB dyad axis, in etoposide-treated *S. cerevisiae*. The position of the flanking regions (F.R.) identified in Gyrase

979 mapping experiments, and the flanking regions observed here for Top2 are indicated in blue and
980 black, respectively.
981 **D)** Average nucleotide composition over a 120 bp window centred on the DSB dyad axis, in
982 etoposide-treated *S. cerevisiae*. The signal pattern is separated into A+T and G+C (top left and right),
983 and into individual A, T, C and G plots (middle left, bottom left, middle right, and bottom right,
984 respectively). The position of the flanking regions (F.R.) observed here for Top2 are indicated in
985 black, and their ~10.5 bp periodicity is highlighted with black and red crosses.
986
987 **Figure S4. CC-seq maps of TOP2-linked DNA breaks in Human cells are enriched by**
988 **etoposide, and show high reproducibility and nucleotide accuracy (related to Figure 3)**
989 **A)** Broad-scale *H. sapiens* TOP2 CC-seq maps in individual biological replicates of RPE-1 cells
990 ±VP16. Raw data were binned at 100 Kbp prior to plotting. Each plot is offset on the y-axis by +0.3
991 HpB.
992 **B)** Replicate-to-replicate Pearson correlation values (r) for 10 Kbp binned TOP2 CC-seq maps of
993 RPE-1 cells ±VP16.
994 **C)** Scatter plot of -VP16 and +VP16 TOP2 CC-seq maps binned at 10 Kbp resolution. Data were first
995 scaled according to the estimated noise fraction (**Methods**), and are presented in a hexagonal-
996 binned format, where the density of overplotting is indicated by the colour scale.
997 **D)** Violin plots of TOP2 CC-seq maps ±VP16 binned at 100 Kbp resolution. The inner black bar,
998 black dot, and dotted horizontal line indicate the interquartile range, median, and expected mean
999 Top2 CC density based on random distribution.
1000 **E)** The normalised number of TOP2 CCs retained in the CC-seq maps in RPE-1 cells ±VP16 after
1001 filtering to include only sites offset by the given number of base pairs. Data were normalised over a -
1002 100 to +100 bp window.
1003
1004 **Figure S5. CC-seq signal is TOP2-dependent**
1005 **A)** DNA content histograms of wild type (WT) and *TOP2B*$^{-/-}$ RPE-1 cells under asynchronous (10%
1006 FCS) and serum-deprived (0% FCS) conditions, as measured by FACS following propidium iodide
1007 (PI) staining. G1, S and G2 populations are clearly present under asynchronous growing conditions.
1008 A strong G1 arrest is observed in serum deprived conditions. Percentages of cells in each of the
1009 indicated regions (red dotted brackets) are given.
1010 **B)** Western blots demonstrating the absence of TOP2β protein in serum deprived and asynchronous
1011 *TOP2B*$^{-/-}$ RPE-1 cells (left), and the absence of TOP2α in serum deprived wild type and *TOP2B*$^{-/-}$
1012 RPE-1 cells (right). Ponceau S total protein loading is presented (Pon. S) for the left and right panels,
1013 and additionally a Ku80 loading control is included for the right panel.
1014 **C)** Immunofluorescence experiment demonstrating induction of γ-H2AX foci (green) in asynchronous
1015 (Async.) and serum-deprived (Ser. Dep.) wild type (WT) and *TOP2B*$^{-/-}$ RPE-1 cells, all co-stained with
1016 DAPI (blue). Galleries of nine cells per condition were chosen randomly using Olympus ScanR
1017 Analysis software.
1018 **D)** Quantification of (C). Numbers of γ-H2AX foci per cell were counted automatically using Olympus
1019 ScanR Analysis software. The mean ±SEM is reported for n= 3 biological replicate experiments.
1020 **E)** Broad-scale *H. sapiens* TOP2 CC-seq maps in asynchronous and serum-deprived wild type (WT)
1021 and *TOP2B*$^{-/-}$ RPE-1 cells -VP16 (orange) and +VP16 (green). Raw hits on Watson and Crick strands
1022 were summed and smoothed according to local signal density (Fsize=501).
1023
1024 **Figure S6. TOP2 CC-seq signal enrichment around CTCF and TSS sites, compared with END-**
1025 **seq DSB signal at TSSs**
1026 **A)** Fine-scale TOP2 CC-seq maps of *H. sapiens* CTCF-proximal loci in RPE-1 cells +VP16. Red and
1027 blue traces indicate TOP2-linked 5' DNA termini on the Watson and Crick strands, respectively. Pale
1028 shaded areas are the same data smoothed with a sliding 11 bp Hanning window. Red and Blue

rectangles indicate the positions of CTCF motifs on the Watson and Crick strands respectively. The grey line indicates Hanning-smoothed sum of Watson and Crick TOP2 CCs.

B) Fine-scale mapping of TOP2 CCs surrounding three complex CTCF loci, processed as in (A).

C) Aggregation of TOP2 CCs in a 1 Kbp window centred on the subset of orientated CTCF motifs that can be assigned to a chromatin loop anchor in human RPE-1 cells (Darrow et al., 2016). Motifs are stratified into 4 quartiles of loop anchor interaction strength, and the average TOP2 CC distribution in each quartile plotted.

D) Fine-scale aggregation of TOP2 CCs (red) in a 800 bp window centred on TSSs in human RPE-1 cells, showing anticorrelation with aggregated MNase-seq signal (blue).

E) Aggregation of END-seq mapped DSBs in a 10 Kbp window centred on orientated TSSs in human MCF7 cells. Four example TSSs are shown orientated in the 5'-3' direction (top). A heatmap of all TSSs in the human genome, with 25 rows stratified by flanking gene expression level in MCF7 cells (middle). The colour scale indicates average END-seq DSB density. TSSs are also stratified into 4 quartiles based on strength of flanking gene expression, and the average END-seq DSB distribution in each quartile plotted (bottom).

Figure S7. TSS-proximal TOP2-linked DNA breaks in humans are correlated with gene length, independently from gene expression level (related to Figure 5); TSS-proximal Top2-linked DNA breaks in yeast are not strongly correlated with gene length, (related to Figure 2)

A) Aggregation of TOP2 CCs in a 10 Kbp window centred on orientated TSSs in human RPE-1 cells. A heatmap of all TSSs in the human genome, with 25 rows stratified by gene length (top). The colour scale indicates average TOP2 CC density. Motifs are also stratified into 4 quartiles of gene length, and the average TOP2 CC distribution in each quartile plotted (bottom).

B) Aggregation of Top2 CCs in a 10 Kbp window centred on orientated transcription start sites (TSS) in *pdr1*Δ *S. cerevisiae*. Heatmap of all TSSs in the *S. cerevisiae* genome, with 25 rows stratified by gene length level (top). Colour scale indicates average Top2 CC density. Motifs are also stratified into four quartiles of gene length, and the average distribution of Top2 CCs in each quartile plotted (bottom).

C) Scatter plot of human gene length and RPE-1 gene expression, showing no correlation.

D) Scatter plot of *S. cerevisiae* gene length and gene expression during vegetative growth, showing little correlation.

Supplementary Tables

Table S1. DNA libraries used for mapping Spo11 activity. The number of reads remaining after each stage of the data pipeline are indicated.

Species	Strain/ Cell line	Condition	NGS Platform	Library code	Total Read Pairs	Mapped reads	Blacklist-filtered reads	% of Total
S. cerevisiae	*sae2*Δ	Meiosis	MiSeq	1	3512089	3376630	3177210	90.5
				2A	10101423	8796998	8564017	84.8
				3	4957477	4745192	4502308	90.8
				5	4012972	3705100	3559541	88.7
				7BC	4065600	3779390	3569290	87.8

1073 **Table S2. DNA libraries used for mapping Top2 activity.** The number of reads
1074 remaining after each stage of the data pipeline are indicated.
1075

Species	Strain/ Cell line	Condition	NGS Platform	Library code	Total Read Pairs	Mapped reads	De-duplicated reads	Blacklist-filtered reads	% of Total	Pooled Reads (Millions)
S. cerevisiae	*pdr1Δ*	-VP16	NextSeq 500	RA1	3741251	3542955	3179049	2746294	73.4	3.50
			MiSeq	RA8	1118483	879107	842290	751850	67.2	
S. cerevisiae	*pdr1Δ*	+VP16	NextSeq 500	RA2	3096257	3053356	2679303	2234941	72.2	3.93
			MiSeq	RA9	2262958	2071231	1958341	1690075	74.7	
S. cerevisiae	*pdr1Δ sae2Δ*	-VP16	NextSeq 500	RA4	3634284	3552818	3215523	2745668	75.5	3.79
			MiSeq	RA10	1420662	1214067	1181399	1046827	73.7	
S. cerevisiae	*pdr1Δ sae2Δ*	+VP16	NextSeq 500	RA5	2529368	2476714	1386551	1097282	43.4	3.54
			MiSeq	RA11	3226626	3063388	2824882	2444486	75.8	
S. cerevisiae	*pdr1Δ mre11Δ*	-VP16	NextSeq 500	RA6	5345587	5205411	4288662	3646842	68.2	4.76
			MiSeq	RA12	1519020	1326435	1280137	1109310	73.0	
S. cerevisiae	*pdr1Δ mre11Δ*	+VP16	NextSeq 500	RA7	3382546	3357168	2921333	2526342	74.7	5.54
			MiSeq	RA13	4133347	4032996	3540366	3010542	72.8	
Human	RPE-1 WT	-VP16	NextSeq 500	WG11	125203096	109503841	68845619	68639594	54.8	185.36
				WG15	125328792	110432447	46588296	46449378	37.1	
				WG23	89154181	77728045	70484665	70269334	78.8	
Human	RPE-1 WT	+VP16	NextSeq 500	WG12	110910655	95546007	55848200	55681939	50.2	276.97
				WG16	102804692	91872706	54312084	54164650	52.7	
				WG24	130816235	114086421	101162102	100857557	77.1	
				WG34	91829516	79751337	66458538	66270349	72.2	
Human	RPE-1 WT	-VP16 G1	MiSeq	WG13	2601642	2292863	2007177	1991088	76.5	4.27
				WG21	2610523	2298289	2295625	2277124	87.2	
Human	RPE-1 WT	+VP16 G1	MiSeq	WG14	3075620	2771819	2491674	2475350	80.5	5.23
				WG22	3139164	2779809	2772349	2751281	87.6	
Human	RPE-1 WT	-VP16 Async	MiSeq	WG15b*	3207507	2866283	2782876	2760652	86.1	5.35
				WG23	2959289	2616954	2608670	2586523	87.4	
Human	RPE-1 WT	+VP16 Async	MiSeq	WG16b*	3018163	2721770	2673273	2656580	88.0	6.30
				WG24	4165048	3682708	3668602	3639324	87.4	
Human	RPE-1 TOP2B-	-VP16 G1	MiSeq	WG17	2978044	2624262	2558332	2536752	85.2	4.69
				WG25	2460949	2181002	2173777	2155101	87.6	
Human	RPE-1 TOP2B-	+VP16 G1	MiSeq	WG18	2927745	2588870	2557532	2537085	86.7	5.10
				WG26	2922624	2596547	2587152	2565454	87.8	
Human	RPE-1 TOP2B-	-VP16 Async	MiSeq	WG19	3713068	3278164	3188049	3162895	85.2	7.04
				WG27	4413242	3943962	3910035	3877611	87.9	
Human	RPE-1 TOP2B-	+VP16 Async	MiSeq	WG20	3426100	3038601	2978047	2956076	86.3	8.13
				WG28	5878342	5251089	5211027	5169010	87.9	

1076
1077
1078

Table S3. *S. cerevisiae* strains used in this study. Strains MJ315 and M319 were used for Spo11 mapping; strains MJ429, MJ475 and MJ551 were used for Top2 mapping.

Strain	Number	Genotype
sae2Δ	MJ315	SK1: *ho::LYS2/', lys2/', ura3/', arg4-nsp/', leu2::hisG/', his4X::LEU2/', nuc1::LEU2/', sae2Δ::KanMX6/'*
sae2Δ spo11-Y135F	MJ319	SK1: *ho::LYS2/', lys2/', ura3/', arg4-nsp/', leu2::hisG/', his4X::LEU2/', nuc1::LEU2/', spo11(Y135F)-HA3His6::KanMX4/', sae2Δ::KanMX6/'*
pdr1Δ	MJ429	BY4741: *ura3Δ0, leu2Δ0, his3Δ1, met15Δ0, pdr1Δ::PDR1-DBD-CYC8::LEU2*
pdr1Δ sae2Δ	MJ475	BY4741: *ura3Δ0, leu2Δ0, his3Δ1, met15Δ0, pdr1Δ::PDR1-DBD-CYC8::LEU2, sae2Δ::KanMX6*
pdr1Δ mre11Δ	MJ551	BY4741: *ura3Δ0, leu2Δ0, his3Δ1, met15Δ0, pdr1Δ::PDR1-DBD-CYC8::LEU2, mre11Δ::KanMX4*

Table S4. Human cell lines used in this study.

Parent cell line	Clone number	Genotype
hTERT RPE-1	WT	WT
hTERT RPE-1	T2B/1	*TOP2B*

Table S5. The annealed structures of the custom P5 and P7 adapters. "T_i" indicates an inverted dT, linked via a 3'-3' phosphodiester. This inhibits unwanted ligation at this end of the adapter. Also note that the 5'-terminal moieties of each adapter (A for P5, G for P7) are nucleosides (3'-OH), which further inhibits ligation at this end

Adapter	Annealed Structure
P5	blocked end ACACTCTTTCCCTACACGACGCTCTTCCGATCT T_iTGTGAGAAAGGGATGTGCTGCGAGAAGGCTAGp ligated end
P7	ligated end pGATCGGAAGAGCACACGTCTGAACTCCAGTCACT$_i$ TCTAGCCTTCTCGTGTGCAGACTTGAGGTCAGTG blocked end

Table S6. Publically available datasets used in this study.

Species/ Cell line	Dataset Type	Accession(s)	Reference
S. cerevisiae / SK1 (meiotic)	Gene expression microarray	GSM907178, GSM90719, GSM907180	(Dominissini et al., 2012)
S. cerevisiae / SK1 (vegetative)	Gene expression microarray	GSM907176, GSM907177	(Dominissini et al., 2012)
H. sapiens / RPE-1	Gene expression microarray	GSM1395252, GSM1395253, GSM1395254	(Ganem et al., 2014)
H. Sapiens / MCF7	Gene expression microarray	GSM1141244	(Nelson et al., 2013)
H. sapiens / RPE-1	Hi-C	GSE71831	(Darrow et al., 2016)
H. sapiens / RPE-1	bTMP-seq	GSM1062645, GSM1062646	(Naughton et al., 2013)
H. sapiens / MCF7	END-seq	GSM2635568	(Canela et al., 2017)
H. sapiens / RPE-1	CTCF ChIP-seq	GSM749673, GSM1022665	(ENCODE, 2012)
H. sapiens / RPE-1	H3K4Me3 ChIP-seq	GSM945271, GSM945271	(ENCODE, 2012)
H. sapiens / RPE-1	H3K27Ac ChIP-seq	GSM733771, GSM733718, GSM733755, GSM733691, GSM733656, GSM733674, GSM733646	(ENCODE, 2012)
H. sapiens / RPE-1	Methyl-RRBS	GSM683773, GSM683905	(ENCODE, 2012)
H. sapiens / K562	MNase-seq	GSM920557	(ENCODE, 2012)

References

Akimitsu, N., Adachi, N., Hirai, H., Hossain, M. S., Hamamoto, H., Kobayashi, M., Aratani, Y., Koyama, H., and Sekimizu, K. (2003). Enforced cytokinesis without complete nuclear division in embryonic cells depleting the activity of DNA topoisomerase IIalpha. Genes Cells *8*, 393-402.

Anand, R., Ranjha, L., Cannavo, E., and Cejka, P. (2016). Phosphorylated CtIP Functions as a Co-factor of the MRE11-RAD50-NBS1 Endonuclease in DNA End Resection. Mol Cell *64*, 940-950.

Austin, C. A., Lee, K. C., Swan, R. L., Khazeem, M. M., Manville, C. M., Cridland, P., Treumann, A., Porter, A., Morris, N. J., and Cowell, I. G. (2018). TOP2B: The First Thirty Years. Int J Mol Sci *19*,

Baranello, L., Kouzine, F., Wojtowicz, D., Cui, K., Przytycka, T. M., Zhao, K., and Levens, D. (2014). DNA break mapping reveals topoisomerase II activity genome-wide. Int J Mol Sci *15*, 13111-13122.

Baxter, J., and Diffley, J. F. (2008). Topoisomerase II inactivation prevents the completion of DNA replication in budding yeast. Mol Cell *30*, 790-802.

Bergerat, A., de Massy, B., Gadelle, D., Varoutas, P. C., Nicolas, A., and Forterre, P. (1997). An atypical topoisomerase II from Archaea with implications for meiotic recombination. Nature *386*, 414-417.

Bermejo, R., Capra, T., Gonzalez-Huici, V., Fachinetti, D., Cocito, A., Natoli, G., Katou, Y., Mori, H., Kurokawa, K., Shirahige, K., and Foiani, M. (2009). Genome-organizing factors Top2 and Hmo1 prevent chromosome fragility at sites of S phase transcription. Cell *138*, 870-884.

Borgnetto, M. E., Zunino, F., Tinelli, S., Kas, E., and Capranico, G. (1996). Drug-specific sites of topoisomerase II DNA cleavage in Drosophila chromatin: heterogeneous localization and reversibility. Cancer Res *56*, 1855-1862.

Brill, S. J., DiNardo, S., Voelkel-Meiman, K., and Sternglanz, R. (1987). Need for DNA topoisomerase activity as a swivel for DNA replication for transcription of ribosomal RNA. Nature *326*, 414-416.

Bromberg, K. D., Burgin, A. B., and Osheroff, N. (2003). A two-drug model for etoposide action against human topoisomerase IIalpha. J Biol Chem *278*, 7406-7412.

Canela, A., Maman, Y., Jung, S., Wong, N., Callen, E., Day, A., Kieffer-Kwon, K.-R., Pekowska, A., Zhang, H., Rao, S. S. P., Huang, S.-C., Mckinnon, P. J., Aplan, P. D., Pommier, Y., Aiden, E. L., Casellas, R., and Nussenzweig, A. (2017). Genome Organization Drives Chromosome Fragility. Cell *170*, 507-521.e18.

Cannavo, E., Johnson, D., Andres, S. N., Kissling, V. M., Reinert, J. K., Garcia, V., Erie, D. A., Hess, D., Thomä, N. H., Enchev, R. I., Peter, M., Williams, R. S., Neale, M. J., and Cejka, P. (2018). Regulatory control of DNA end resection by Sae2 phosphorylation. Nat Commun *9*, 4016.

Cannavo, E., and Cejka, P. (2014). Sae2 promotes dsDNA endonuclease activity within Mre11-Rad50-Xrs2 to resect DNA breaks. Nature *514*, 122-125.

Capranico, G., Jaxel, C., Roberge, M., Kohn, K. W., and Pommier, Y. (1990). Nucleosome positioning as a critical determinant for the DNA cleavage sites of mammalian DNA topoisomerase II in reconstituted simian virus 40 chromatin. Nucleic Acids Res *18*, 4553-4559.

Chen, G. L., Yang, L., Rowe, T. C., Halligan, B. D., Tewey, K. M., and Liu, L. F. (1984). Nonintercalative antitumor drugs interfere with the breakage-reunion reaction of mammalian DNA topoisomerase II. J Biol Chem *259*, 13560-13566.

Coombs, D. H., and Pearson, G. D. (1978). Filter-binding assay for covalent DNA-protein complexes: adenovirus DNA-terminal protein complex. Proc Natl Acad Sci U S A *75*, 5291-5295.

Cortes Ledesma, F., El Khamisy, S. F., Zuma, M. C., Osborn, K., and Caldecott, K. W. (2009). A human 5'-tyrosyl DNA phosphodiesterase that repairs topoisomerase-mediated DNA damage. Nature *461*, 674-678.

Cowell, I. G., Sondka, Z., Smith, K., Lee, K. C., Manville, C. M., Sidorczuk-Lesthuruge, M., Rance, H. A., Padget, K., Jackson, G. H., Adachi, N., and Austin, C. A. (2012). Model for MLL translocations in therapy-related leukemia involving topoisomerase IIβ-mediated DNA strand breaks and gene proximity. Proc Natl Acad Sci U S A *109*, 8989-8994.

Crosetto, N., Mitra, A., Silva, M. J., Bienko, M., Dojer, N., Wang, Q., Karaca, E., Chiarle, R., Skrzypczak, M., Ginalski, K., Pasero, P., Rowicka, M., and Dikic, I. (2013). Nucleotide-resolution DNA double-strand break mapping by next-generation sequencing. Nat Methods *10*, 361-365.

Darrow, E. M., Huntley, M. H., Dudchenko, O., Stamenova, E. K., Durand, N. C., Sun, Z., Huang, S. C., Sanborn, A. L., Machol, I., Shamim, M., Seberg, A. P., Lander, E. S., Chadwick, B. P., and Aiden, E. L. (2016). Deletion of DXZ4 on the human inactive X chromosome alters higher-order genome architecture. Proc Natl Acad Sci U S A *113*, E4504-12.

Deweese, J. E., and Osheroff, N. (2009). The DNA cleavage reaction of topoisomerase II: wolf in sheep's clothing. Nucleic Acids Res *37*, 738-748.

DiNardo, S., Voelkel, K., and Sternglanz, R. (1984). DNA topoisomerase II mutant of Saccharomyces cerevisiae: topoisomerase II is required for segregation of daughter molecules at the termination of DNA replication. Proc Natl Acad Sci U S A *81*, 2616-2620.

Dominissini, D., Moshitch-Moshkovitz, S., Schwartz, S., Salmon-Divon, M., Ungar, L., Osenberg, S., Cesarkas, K., Jacob-Hirsch, J., Amariglio, N., Kupiec, M., Sorek, R., and Rechavi, G. (2012). Topology of the human and mouse m6A RNA methylomes revealed by m6A-seq. Nature *485*, 201-206.

Durand, N. C., Shamim, M. S., Machol, I., Rao, S. S., Huntley, M. H., Lander, E. S., and Aiden, E. L. (2016). Juicer Provides a One-Click System for Analyzing Loop-Resolution Hi-C Experiments. Cell Syst *3*, 95-98.

ENCODE, P. C. (2012). An integrated encyclopedia of DNA elements in the human genome. Nature *489*, 57-74.

Ganem, N. J., Cornils, H., Chiu, S. Y., O'Rourke, K. P., Arnaud, J., Yimlamai, D., Théry, M., Camargo, F. D., and Pellman, D. (2014). Cytokinesis failure triggers hippo tumor suppressor pathway activation. Cell *158*, 833-848.

1163 Garcia, V., Phelps, S. E. L., Gray, S., and Neale, M. J. (2011). Bidirectional resection of DNA double-strand breaks by Mre11
1164 and Exo1. Nature *479*, 241-244.
1165 Gómez-Herreros, F., Schuurs-Hoeijmakers, J. H., McCormack, M., Greally, M. T., Rulten, S., Romero-Granados, R., Counihan,
1166 T. J., Chaila, E., Conroy, J., Ennis, S., Delanty, N., Cortés-Ledesma, F., de Brouwer, A. P., Cavalleri, G. L., El-Khamisy, S. F.,
1167 de Vries, B. B., and Caldecott, K. W. (2014). TDP2 protects transcription from abortive topoisomerase activity and is required
1168 for normal neural function. Nat Genet *46*, 516-521.
1169 Gothe, H. J., Bouwman, B. A. M., Gusmao, E. G., Piccinno, R., Sayols, S., Drechsel, O., Petrosino, G., Minneker, V., Josipovic,
1170 N., Mizi, A., Nielsen, C. F., Wagner, E.-M., Takeda, S., Sasanuma, H., Hudson, D. F., Kindler, T., Baranello, L., Papantonis, A.,
1171 Crosetto, N., and Roukos, V. (2018). Spatial chromosome folding and active transcription drive DNA fragility and formation of
1172 oncogenic MLL translocations. bioRxiv *http://dx.doi.org/10.1101/485763*,
1173 Grant, C. E., Bailey, T. L., and Noble, W. S. (2011). FIMO: scanning for occurrences of a given motif. Bioinformatics *27*, 1017-
1174 1018.
1175 Grue, P., Grässer, A., Sehested, M., Jensen, P. B., Uhse, A., Straub, T., Ness, W., and Boege, F. (1998). Essential mitotic
1176 functions of DNA topoisomerase IIalpha are not adopted by topoisomerase IIbeta in human H69 cells. J Biol Chem *273*, 33660-
1177 33666.
1178 Grzybowski, A. T., Chen, Z., and Ruthenburg, A. J. (2015). Calibrating ChIP-Seq with Nucleosomal Internal Standards to
1179 Measure Histone Modification Density Genome Wide. Mol Cell *58*, 886-899.
1180 Haffner, M. C., Aryee, M. J., Toubaji, A., Esopi, D. M., Albadine, R., Gurel, B., Isaacs, W. B., Bova, G. S., Liu, W., Xu, J.,
1181 Meeker, A. K., Netto, G., De Marzo, A. M., Nelson, W. G., and Yegnasubramanian, S. (2010). Androgen-induced TOP2B-
1182 mediated double-strand breaks and prostate cancer gene rearrangements. Nat Genet *42*, 668-675.
1183 Hamilton, N. K., and Maizels, N. (2010). MRE11 function in response to topoisomerase poisons is independent of its function in
1184 double-strand break repair in Saccharomyces cerevisiae. PLoS One *5*, e15387.
1185 Hartsuiker, E., Neale, M. J., and Carr, A. M. (2009). Distinct requirements for the Rad32(Mre11) nuclease and Ctp1(CtIP) in the
1186 removal of covalently bound topoisomerase I and II from DNA. Mol Cell *33*, 117-123.
1187 Heck, M. M., Hittelman, W. N., and Earnshaw, W. C. (1988). Differential expression of DNA topoisomerases I and II during the
1188 eukaryotic cell cycle. Proc Natl Acad Sci U S A *85*, 1086-1090.
1189 Hoa, N. N., Shimizu, T., Zhou, Z. W., Wang, Z. Q., Deshpande, R. A., Paull, T. T., Akter, S., Tsuda, M., Furuta, R., Tsusui, K.,
1190 Takeda, S., and Sasanuma, H. (2016). Mre11 Is Essential for the Removal of Lethal Topoisomerase 2 Covalent Cleavage
1191 Complexes. Mol Cell *64*, 580-592.
1192 Hoffman, M. M., Ernst, J., Wilder, S. P., Kundaje, A., Harris, R. S., Libbrecht, M., Giardine, B., Ellenbogen, P. M., Bilmes, J. A.,
1193 Birney, E., Hardison, R. C., Dunham, I., Kellis, M., and Noble, W. S. (2013). Integrative annotation of chromatin elements from
1194 ENCODE data. Nucleic Acids Res *41*, 827-841.
1195 Holm, C., Goto, T., Wang, J. C., and Botstein, D. (1985). DNA topoisomerase II is required at the time of mitosis in yeast. Cell
1196 *41*, 553-563.
1197 Hornyak, P., Askwith, T., Walker, S., Komulainen, E., Paradowski, M., Pennicott, L. E., Bartlett, E. J., Brissett, N. C., Raoof, A.,
1198 Watson, M., Jordan, A. M., Ogilvie, D. J., Ward, S. E., Atack, J. R., Pearl, L. H., Caldecott, K. W., and Oliver, A. W. (2016).
1199 Mode of action of DNA-competitive small molecule inhibitors of tyrosyl DNA phosphodiesterase 2. Biochem J *473*, 1869-1879.
1200 Hsiang, Y. H., Lihou, M. G., and Liu, L. F. (1989). Arrest of replication forks by drug-stabilized topoisomerase I-DNA cleavable
1201 complexes as a mechanism of cell killing by camptothecin. Cancer Res *49*, 5077-5082.
1202 Hsu, P. D., Scott, D. A., Weinstein, J. A., Ran, F. A., Konermann, S., Agarwala, V., Li, Y., Fine, E. J., Wu, X., Shalem, O.,
1203 Cradick, T. J., Marraffini, L. A., Bao, G., and Zhang, F. (2013). DNA targeting specificity of RNA-guided Cas9 nucleases. Nat
1204 Biotechnol *31*, 827-832.
1205 Hu, B., Petela, N., Kurze, A., Chan, K.-L., Chapard, C., and Nasmyth, K. (2015). Biological chromodynamics: a general method
1206 for measuring protein occupancy across the genome by calibrating ChIP-seq. Nucleic Acids Res
1207 Huang, W. C., Lee, C. Y., and Hsieh, T. S. (2017). Single-molecule Förster resonance energy transfer (FRET) analysis
1208 discloses the dynamics of the DNA-topoisomerase II (Top2) interaction in the presence of TOP2-targeting agents. J Biol Chem
1209 *292*, 12589-12598.
1210 Johnson, D., Allison, R. M., Cannavo, E., Cejka, P., and Neale, M. (2019). Removal of Spo11 from meiotic DNA breaks in vitro
1211 but not in vivo by Tyrosyl DNA Phosphodiesterase 2. bioRxiv *http://dx.doi.org/10.1101/527333*,
1212 Käs, E., and Laemmli, U. K. (1992). In vivo topoisomerase II cleavage of the Drosophila histone and satellite III repeats: DNA
1213 sequence and structural characteristics. EMBO J *11*, 705-716.
1214 Keeney, S., Giroux, C. N., and Kleckner, N. (1997). Meiosis-specific DNA double-strand breaks are catalyzed by Spo11, a
1215 member of a widely conserved protein family. Cell *88*, 375-384.
1216 Keeney, S., and Kleckner, N. (1995). Covalent protein-DNA complexes at the 5' strand termini of meiosis-specific double-strand
1217 breaks in yeast. Proc Natl Acad Sci U S A *92*, 11274-11278.
1218 Khan, Q. A., Kohlhagen, G., Marshall, R., Austin, C. A., Kalena, G. P., Kroth, H., Sayer, J. M., Jerina, D. M., and Pommier, Y.
1219 (2003). Position-specific trapping of topoisomerase II by benzo[a]pyrene diol epoxide adducts: implications for interactions with
1220 intercalating anticancer agents. Proc Natl Acad Sci U S A *100*, 12498-12503.
1221 Kingma, P. S., Corbett, A. H., Burcham, P. C., Marnett, L. J., and Osheroff, N. (1995). Abasic sites stimulate double-stranded
1222 DNA cleavage mediated by topoisomerase II. DNA lesions as endogenous topoisomerase II poisons. J Biol Chem *270*, 21441-
1223 21444.
1224 Lee, M. P., Sander, M., and Hsieh, T. (1989). Nuclease protection by Drosophila DNA topoisomerase II. Enzyme/DNA contacts
1225 at the strong topoisomerase II cleavage sites. J Biol Chem *264*, 21779-21787.
1226 Liang, K., and Keleş, S. (2012). Normalization of ChIP-seq data with control. BMC Bioinformatics *13*, 199.
1227 Lieberman-Aiden, E., van Berkum, N. L., Williams, L., Imakaev, M., Ragoczy, T., Telling, A., Amit, I., Lajoie, B. R., Sabo, P. J.,
1228 Dorschner, M. O., Sandstrom, R., Bernstein, B., Bender, M. A., Groudine, M., Gnirke, A., Stamatoyannopoulos, J., Mirny, L. A.,

1229 Lander, E. S., and Dekker, J. (2009). Comprehensive mapping of long-range interactions reveals folding principles of the
1230 human genome. Science *326*, 289-293.
1231 Lin, C., Yang, L., Tanasa, B., Hutt, K., Ju, B. G., Ohgi, K., Zhang, J., Rose, D. W., Fu, X. D., Glass, C. K., and Rosenfeld, M. G.
1232 (2009). Nuclear receptor-induced chromosomal proximity and DNA breaks underlie specific translocations in cancer. Cell *139*,
1233 1069-1083.
1234 Liu, J., Wu, T. C., and Lichten, M. (1995). The location and structure of double-strand DNA breaks induced during yeast
1235 meiosis: evidence for a covalently linked DNA-protein intermediate. EMBO J *14*, 4599-4608.
1236 Liu, L. F., Rowe, T. C., Yang, L., Tewey, K. M., and Chen, G. L. (1983). Cleavage of DNA by mammalian DNA topoisomerase
1237 II. J Biol Chem *258*, 15365-15370.
1238 Liu, Q., and Wang, J. C. (1999). Similarity in the catalysis of DNA breakage and rejoining by type IA and IIA DNA
1239 topoisomerases. Proc Natl Acad Sci U S A *96*, 881-886.
1240 Long, B. H., Musial, S. T., and Brattain, M. G. (1986). DNA breakage in human lung carcinoma cells and nuclei that are
1241 naturally sensitive or resistant to etoposide and teniposide. Cancer Res *46*, 3809-3816.
1242 Lotito, L., Russo, A., Chillemi, G., Bueno, S., Cavalieri, D., and Capranico, G. (2008). Global transcription regulation by DNA
1243 topoisomerase I in exponentially growing Saccharomyces cerevisiae cells: activation of telomere-proximal genes by TOP1
1244 deletion. J Mol Biol *377*, 311-322.
1245 Mathelier, A., Zhao, X., Zhang, A. W., Parcy, F., Worsley-Hunt, R., Arenillas, D. J., Buchman, S., Chen, C. Y., Chou, A.,
1246 Ienasescu, H., Lim, J., Shyr, C., Tan, G., Zhou, M., Lenhard, B., Sandelin, A., and Wasserman, W. W. (2014). JASPAR 2014:
1247 an extensively expanded and updated open-access database of transcription factor binding profiles. Nucleic Acids Res *42*,
1248 D142-7.
1249 Minocha, A., and Long, B. H. (1984). Inhibition of the DNA catenation activity of type II topoisomerase by VP16-213 and VM26.
1250 Biochem Biophys Res Commun *122*, 165-170.
1251 Nakamura, K., Kogame, T., Oshiumi, H., Shinohara, A., Sumitomo, Y., Agama, K., Pommier, Y., Tsutsui, K. M., Tsutsui, K.,
1252 Hartsuiker, E., Ogi, T., Takeda, S., and Taniguchi, Y. (2010). Collaborative action of Brca1 and CtIP in elimination of covalent
1253 modifications from double-strand breaks to facilitate subsequent break repair. PLoS Genet *6*, e1000828.
1254 Naughton, C., Avlonitis, N., Corless, S., Prendergast, J. G., Mati, I. K., Eijk, P. P., Cockroft, S. L., Bradley, M., Ylstra, B., and
1255 Gilbert, N. (2013). Transcription forms and remodels supercoiling domains unfolding large-scale chromatin structures. Nat
1256 Struct Mol Biol *20*, 387-395.
1257 Neale, M. J., Pan, J., and Keeney, S. (2005). Endonucleolytic processing of covalent protein-linked DNA double-strand breaks.
1258 Nature *436*, 1053-1057.
1259 Negri, C., Chiesa, R., Cerino, A., Bestagno, M., Sala, C., Zini, N., Maraldi, N. M., and Astaldi Ricotti, G. C. (1992). Monoclonal
1260 antibodies to human DNA topoisomerase I and the two isoforms of DNA topoisomerase II: 170- and 180-kDa isozymes. Exp
1261 Cell Res *200*, 452-459.
1262 Nelson, E. R., Wardell, S. E., Jasper, J. S., Park, S., Suchindran, S., Howe, M. K., Carver, N. J., Pillai, R. V., Sullivan, P. M.,
1263 Sondhi, V., Umetani, M., Geradts, J., and McDonnell, D. P. (2013). 27-Hydroxycholesterol links hypercholesterolemia and
1264 breast cancer pathophysiology. Science *342*, 1094-1098.
1265 Nitiss, J. L. (2009). Targeting DNA topoisomerase II in cancer chemotherapy. Nat Rev Cancer *9*, 338-350.
1266 Pan, J., Sasaki, M., Kniewel, R., Murakami, H., Blitzblau, H. G., Tischfield, S. E., Zhu, X., Neale, M. J., Jasin, M., Socci, N. D.,
1267 Hochwagen, A., and Keeney, S. (2011). A Hierarchical Combination of Factors Shapes the Genome-wide Topography of Yeast
1268 Meiotic Recombination Initiation. Cell *144*, 719-731.
1269 Pommier, Y., Capranico, G., Orr, A., and Kohn, K. W. (1991). Local base sequence preferences for DNA cleavage by
1270 mammalian topoisomerase II in the presence of amsacrine or teniposide. Nucleic Acids Res *19*, 5973-5980.
1271 Pommier, Y., Schwartz, R. E., Kohn, K. W., and Zwelling, L. A. (1984). Formation and rejoining of deoxyribonucleic acid
1272 double-strand breaks induced in isolated cell nuclei by antineoplastic intercalating agents. Biochemistry *23*, 3194-3201.
1273 Pommier, Y., Sun, Y., Huang, S. N., and Nitiss, J. L. (2016). Roles of eukaryotic topoisomerases in transcription, replication
1274 and genomic stability. Nat Rev Mol Cell Biol *17*, 703-721.
1275 Reece, R. J., and Maxwell, A. (1991). DNA gyrase: structure and function. Crit Rev Biochem Mol Biol *26*, 335-375.
1276 Rowley, J. D., and Olney, H. J. (2002). International workshop on the relationship of prior therapy to balanced chromosome
1277 aberrations in therapy-related myelodysplastic syndromes and acute leukemia: overview report. Genes Chromosomes Cancer
1278 *33*, 331-345.
1279 Sabourin, M., and Osheroff, N. (2000). Sensitivity of human type II topoisomerases to DNA damage: stimulation of enzyme-
1280 mediated DNA cleavage by abasic, oxidized and alkylated lesions. Nucleic Acids Res *28*, 1947-1954.
1281 Sasanuma, H., Tsuda, M., Morimoto, S., Saha, L. K., Rahman, M. M., Kiyooka, Y., Fujiike, H., Cherniack, A. D., Itou, J., Callen
1282 Moreu, E., Toi, M., Nakada, S., Tanaka, H., Tsutsui, K., Yamada, S., Nussenzweig, A., and Takeda, S. (2018). BRCA1 ensures
1283 genome integrity by eliminating estrogen-induced pathological topoisomerase II-DNA complexes. Proc Natl Acad Sci U S A
1284 *115*, E10642-E10651.
1285 Schalbetter, S. A., Fudenberg, G., Baxter, J., Pollard, K. S., and Neale, M. J. (2018). Principles of Meiotic Chromosome
1286 Assembly. bioRXiv *http://dx.doi.org/10.1101/442038*,
1287 Stepanov, A., Nitiss, K. C., Neale, G., and Nitiss, J. L. (2008). Enhancing drug accumulation in Saccharomyces cerevisiae by
1288 repression of pleiotropic drug resistance genes with chimeric transcription repressors. Mol Pharmacol *74*, 423-431.
1289 Stingele, J., Habermann, B., and Jentsch, S. (2015). DNA-protein crosslink repair: proteases as DNA repair enzymes. Trends
1290 Biochem Sci *40*, 67-71.
1291 Strumberg, D., Nitiss, J. L., Dong, J., Kohn, K. W., and Pommier, Y. (1999). Molecular analysis of yeast and human type II
1292 topoisomerases. Enzyme-DNA and drug interactions. J Biol Chem *274*, 28246-28255.
1293 Sun, X., Huang, L., Markowitz, T. E., Blitzblau, H. G., Chen, D., Klein, F., and Hochwagen, A. (2015). Transcription dynamically
1294 patterns the meiotic chromosome-axis interface. Elife *4*,

Sutormin, D., Rubanova, N., Logacheva, M., Ghilarov, D., and Severinov, K. (2018). Single-nucleotide-resolution mapping of DNA gyrase cleavage sites across the Escherichia coli genome. Nucleic Acids Res

Thomsen, B., Bendixen, C., Lund, K., Andersen, A. H., Sørensen, B. S., and Westergaard, O. (1990). Characterization of the interaction between topoisomerase II and DNA by transcriptional footprinting. J Mol Biol *215*, 237-244.

Tiwari, V. K., Burger, L., Nikoletopoulou, V., Deogracias, R., Thakurela, S., Wirbelauer, C., Kaut, J., Terranova, R., Hoerner, L., Mielke, C., Boege, F., Murr, R., Peters, A. H., Barde, Y. A., and Schübeler, D. (2012). Target genes of Topoisomerase IIβ regulate neuronal survival and are defined by their chromatin state. Proc Natl Acad Sci U S A *109*, E934-43.

Udvardy, A., and Schedl, P. (1991). Chromatin structure, not DNA sequence specificity, is the primary determinant of topoisomerase II sites of action in vivo. Mol Cell Biol *11*, 4973-4984.

Uemura, T., and Yanagida, M. (1984). Isolation of type I and II DNA topoisomerase mutants from fission yeast: single and double mutants show different phenotypes in cell growth and chromatin organization. EMBO J *3*, 1737-1744.

Uusküla-Reimand, L., Hou, H., Samavarchi-Tehrani, P., Rudan, M. V., Liang, M., Medina-Rivera, A., Mohammed, H., Schmidt, D., Schwalie, P., Young, E. J., Reimand, J., Hadjur, S., Gingras, A. C., and Wilson, M. D. (2016). Topoisomerase II beta interacts with cohesin and CTCF at topological domain borders. Genome Biol *17*, 182.

Vélez-Cruz, R., Riggins, J. N., Daniels, J. S., Cai, H., Guengerich, F. P., Marnett, L. J., and Osheroff, N. (2005). Exocyclic DNA lesions stimulate DNA cleavage mediated by human topoisomerase II alpha in vitro and in cultured cells. Biochemistry *44*, 3972-3981.

Wang, J. C. (2009). Untangling the double helix Cold Spring Harbor Laboratory Pr).

Wang, Y., Knudsen, B. R., Bjergbaek, L., Westergaard, O., and Andersen, A. H. (1999). Stimulated activity of human topoisomerases IIalpha and IIbeta on RNA-containing substrates. J Biol Chem *274*, 22839-22846.

Wang, Y., Thyssen, A., Westergaard, O., and Andersen, A. H. (2000). Position-specific effect of ribonucleotides on the cleavage activity of human topoisomerase II. Nucleic Acids Res *28*, 4815-4821.

Woessner, R. D., Mattern, M. R., Mirabelli, C. K., Johnson, R. K., and Drake, F. H. (1991). Proliferation- and cell cycle-dependent differences in expression of the 170 kilodalton and 180 kilodalton forms of topoisomerase II in NIH-3T3 cells. Cell Growth Differ *2*, 209-214.

Wozniak, A. J., and Ross, W. E. (1983). DNA damage as a basis for 4'-demethylepipodophyllotoxin-9-(4,6-O-ethylidene-beta-D-glucopyranoside) (etoposide) cytotoxicity. Cancer Res *43*, 120-124.

Wu, C. C., Li, T. K., Farh, L., Lin, L. Y., Lin, T. S., Yu, Y. J., Yen, T. J., Chiang, C. W., and Chan, N. L. (2011). Structural basis of type II topoisomerase inhibition by the anticancer drug etoposide. Science *333*, 459-462.

Wu, J., and Liu, L. F. (1997). Processing of topoisomerase I cleavable complexes into DNA damage by transcription. Nucleic Acids Res *25*, 4181-4186.

Yan, W. X., Mirzazadeh, R., Garnerone, S., Scott, D., Schneider, M. W., Kallas, T., Custodio, J., Wernersson, E., Li, Y., Gao, L., Federova, Y., Zetsche, B., Zhang, F., Bienko, M., and Crosetto, N. (2017). BLISS is a versatile and quantitative method for genome-wide profiling of DNA double-strand breaks. Nat Commun *8*, 15058.

Yang, F., Kemp, C. J., and Henikoff, S. (2015). Anthracyclines induce double-strand DNA breaks at active gene promoters. Mutat Res *773*, 9-15.

Yu, X., Davenport, J. W., Urtishak, K. A., Carillo, M. L., Gosai, S. J., Kolaris, C. P., Byl, J. A. W., Rappaport, E. F., Osheroff, N., Gregory, B. D., and Felix, C. A. (2017). Genome-wide TOP2A DNA cleavage is biased toward translocated and highly transcribed loci. Genome Res *27*, 1238-1249.

Zwelling, L. A., Michaels, S., Erickson, L. C., Ungerleider, R. S., Nichols, M., and Kohn, K. W. (1981). Protein-associated deoxyribonucleic acid strand breaks in L1210 cells treated with the deoxyribonucleic acid intercalating agents 4'-(9-acridinylamino) methanesulfon-m-anisidide and adriamycin. Biochemistry *20*, 6553-6563.

Figure 1

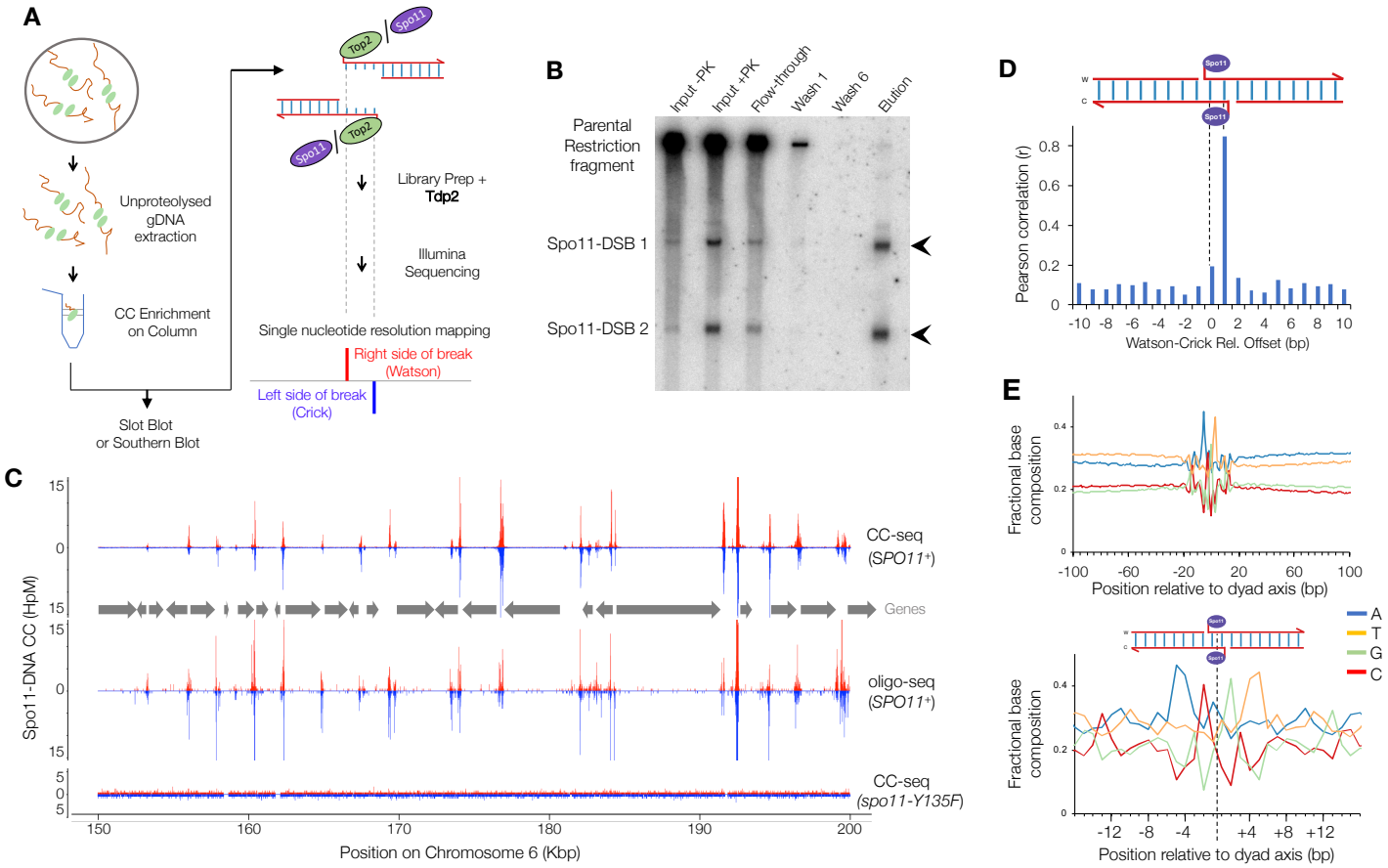

Figure 1. CC-seq maps covalent Spo11-linked DNA breaks in *S. cerevisiae* meiosis with nucleotide accuracy

A) Schematic of the CC-seq method.

B) Column-based enrichment of Spo11-linked DNA fragments detected by Southern blotting at the *his4*::*LEU2* recombination hotspot (**Methods**). Arrows indicate expected sizes of Spo11-DSBs.

C) Nucleotide resolution mapping of *S. cerevisiae* Spo11 hotspots by CC-seq or oligo-seq (Pan et al., 2011). Red and blue traces indicate Spo11-linked 5' DNA termini on the Watson and Crick strands, respectively. Grey arrows indicate positions of gene open reading frames.

D) Pearson correlation (r) of Spo11 CC-seq signal between Watson and Crick strands, offset by the indicated distances.

E) Average nucleotide composition over a 200 (top) and 30 bp (bottom) window centred on Spo11 breaks. Bases reported are for the top strand only.

HpM = Hits per million mapped reads per base pair.

Figure 2

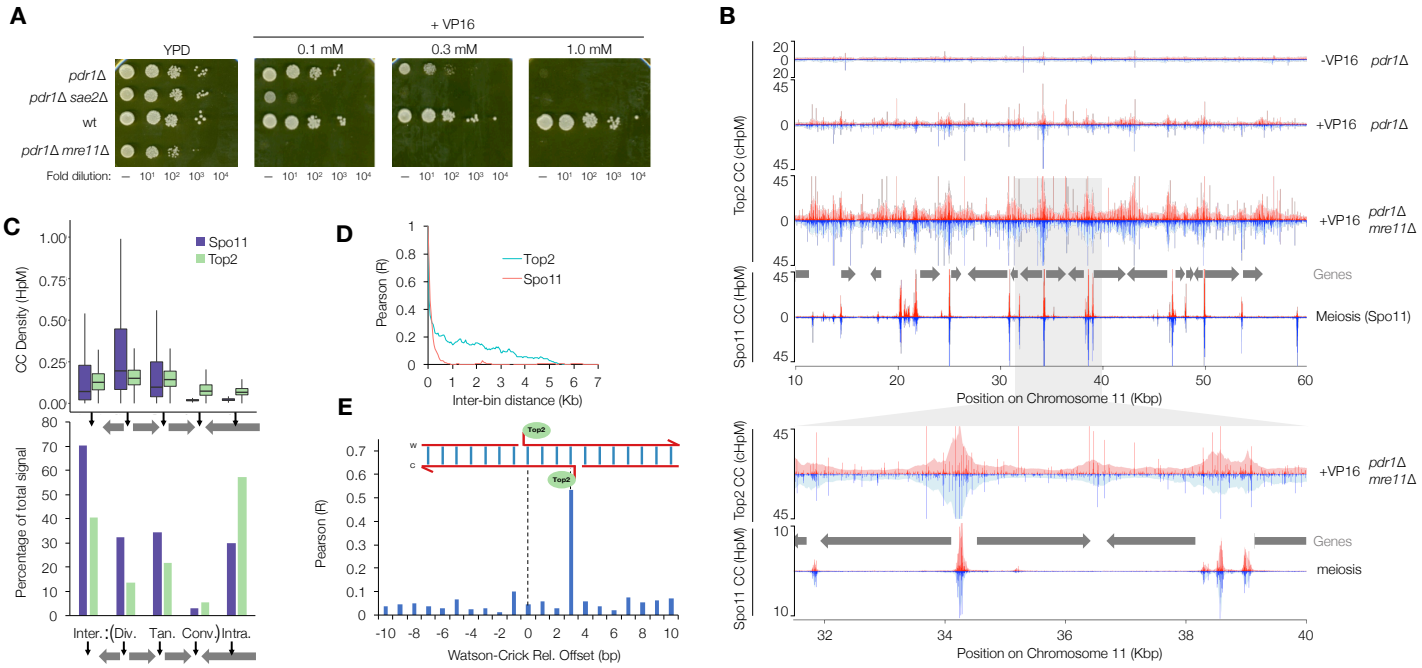

Figure 2. CC-seq maps covalent Top2-linked DNA breaks in *S. cerevisiae* cycling cells with nucleotide accuracy
A) Serial dilution spot tests of VP16 tolerance for the indicated strains.
B) Nucleotide resolution mapping of *S. cerevisiae* Top2 CCs by CC-seq of the indicated strains after treatment for 4 hours with 1 mM VP16. Spo11-CC data is plotted for comparison. Top2 CC data were calibrated using a human DNA spike-in (**Methods**). Red and blue traces indicate CC-linked 5' DNA termini on the Watson and Crick strands, respectively. Grey arrows indicate positions of gene open reading frames. Lower panels show an expanded view of the region from 31.5 to 40 Kbp.
C) Quantification of Top2 and Spo11 CC signal stratified by genomic region. The genome was divided into intra and intergenic regions; the intergenic region was further divided into divergent, tandem and convergent based on orientation of flanking genes. Spo11 and Top2 activity mapped by CC-seq is expressed as box-and-whisker plots of density (upper and lower box limit: 3rd and 1st quartile; bar: median; upper and lower whisker: highest and lowest values within 1.5-fold of the interquartile range), or as the percentage of total mapped reads.
D) Local correlation of Top2 or Spo11 CC-seq signals. Top2 or Spo11 CC-seq data were binned at 50 bp resolution and the Pearson correlation calculated between bins of increasing separation.
E) Pearson correlation (r) of Top2 CC-seq signal on Watson and Crick strands, offset by the indicated distance.
HpM = Hits per million mapped reads per base pair.

Figure 3

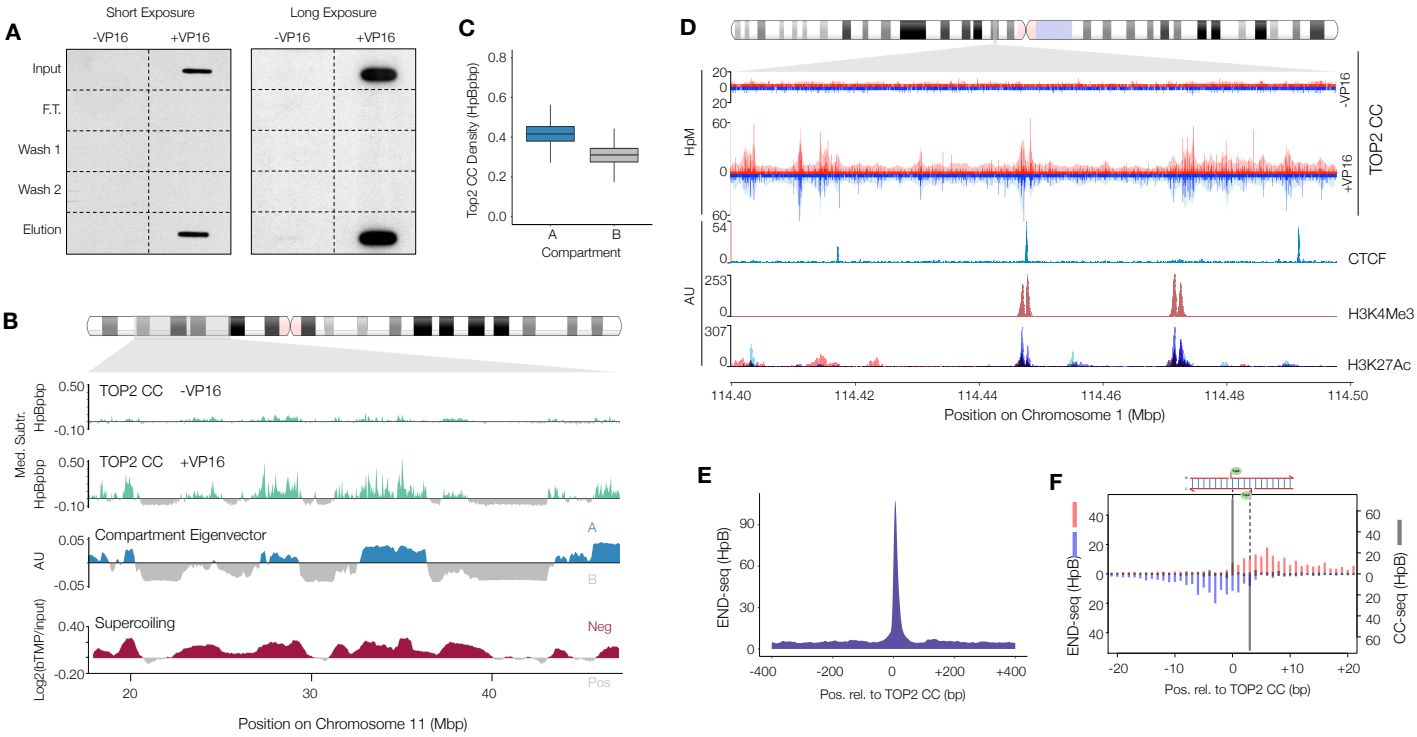

Figure 3. CC-seq maps TOP2-linked DNA breaks in Human cells with nucleotide accuracy

A) Anti-TOP2β western slot blot of input, flow through, wash, and elution fractions. RPE-1 cells were treated or not with VP16, prior to processing according to **Figure 1A**.

B) Broad-scale maps of *H. sapiens* TOP2 CCs produced by CC-seq in RPE-1 cells ±VP16. Raw data were scaled, binned, smoothed and median subtracted prior to plotting (**Methods**). Chromatin compartments revealed by Hi-C eigenvector analysis (Darrow et al., 2016), and supercoiling revealed by bTMP ChIP-seq (Naughton et al., 2013) are shown for comparison.

C) Quantification of TOP2 CC in chromatin compartments A and B. Data are expressed as box-and-whisker plots of density as for **Figure 2C**.

D) Fine-scale mapping of *H. sapiens* TOP2 CCs by CC-seq in RPE-1 cells ±VP16. Red and blue traces indicate TOP2-linked 5' DNA termini on the Watson and Crick strands, respectively. Pale shaded areas are the same data smoothed according to local density (see **Methods**). RPE-1 CTCF and H3K4Me3 ChIP-seq data plus H3K27Ac ChIP-seq data overlaid from seven cell lines (ENCODE, 2012) is shown for comparison.

E) Medium-scale aggregate of END-seq mapped DSBs (Canela et al., 2017) surrounding nucleotide resolution CC-seq mapped TOP2 CCs.

F) Fine-scale strand-specific aggregate of END-seq mapped DSB ends (red and blue bars) and nucleotide resolution CC-seq mapped TOP2 CCs (grey bars) surrounding strong TOP2 CC sites.

Figure 4

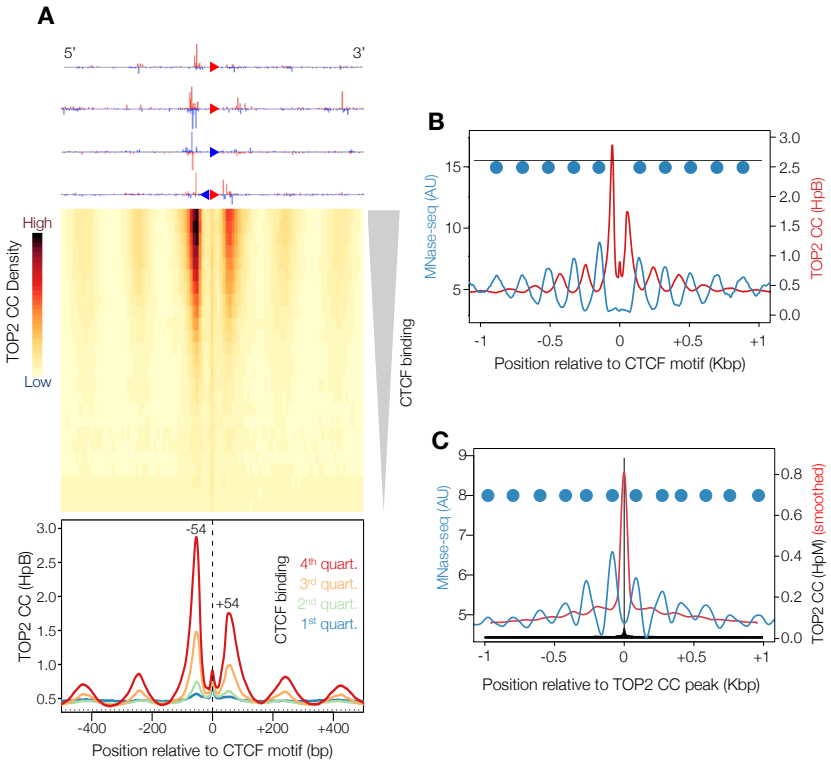

Figure 4. CTCF-proximal TOP2 activity is tightly confined within nucleosome-depleted regions
A) Aggregation of TOP2 CCs in a 1 Kbp window centred on orientated CTCF motifs in human RPE-1 cells. Four example CTCF loci are shown orientated in the 5'-3' direction (top). A heatmap of all CTCF-motifs in the human genome, with 25 rows stratified by the strength of colocalising CTCF ChIP-seq peaks in RPE-1 cells (middle). The colour scale indicates average TOP2 CC density. Motifs are also stratified into 4 quartiles of CTCF-binding, and the average TOP2 CC distribution in each quartile plotted (bottom).
B) Aggregated TOP2 CC distribution (red line) in the highest quartile of CTCF-binding compared with the average MNase-seq signal (blue line).
C) Aggregated TOP2 CC distribution (black and red lines: single-nucleotide resolution and smoothed, respectively) and the average MNase-seq signal (blue line) surrounding strong TOP2 CC sites.
In (B) and (C) peaks in MNase-seq signal indicate inferred nucleosome positions (blue circles).

Figure 5

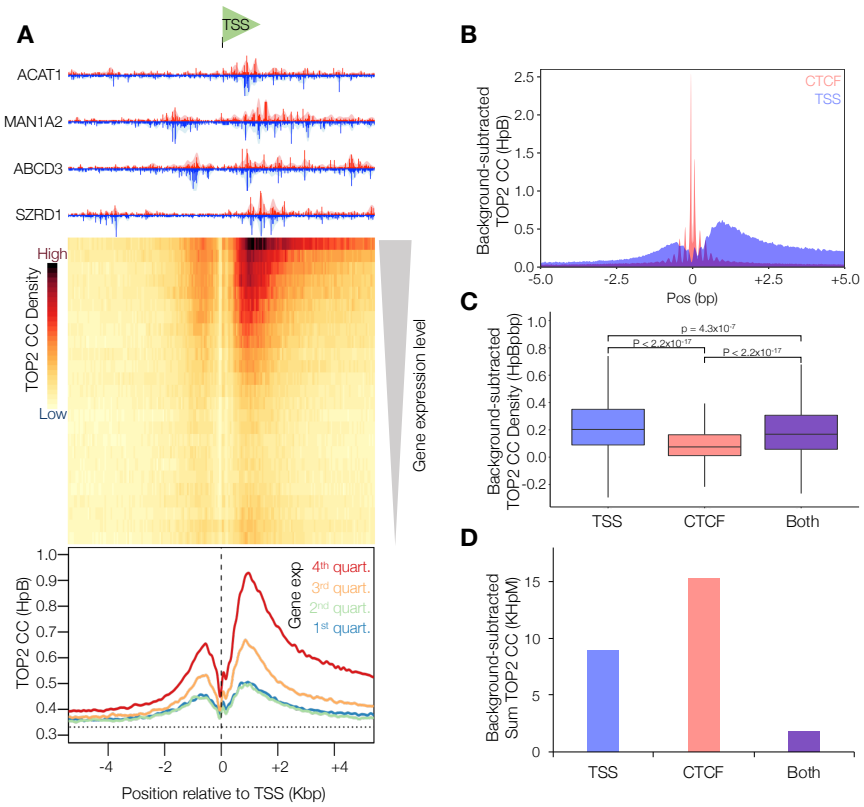

Figure 5. TSS-proximal TOP2 activity is strongly correlated with gene transcription
A) Aggregation of TOP2 CCs in a 10 Kbp window centred on orientated TSSs in human RPE-1 cells. Four example TSSs are shown orientated in the 5'-3' direction (top). A heatmap of all TSSs in the human genome, with 25 rows stratified by gene expression level in RPE-1 cells (middle). The colour scale indicates average TOP2 CC density. Motifs are also stratified into 4 quartiles of gene expression, and the average TOP2 CC distribution in each quartile plotted (bottom).
B) Comparison of CTCF-proximal and TSS-proximal TOP2 CC distributions in the highest quartile of CTCF-binding (pink) and gene-expression (blue), respectively.
C) Average TOP2 CC density in 10 Kbp regions centred on the highest quartile of TSS, CTCF, or regions where both features are present. Data are expressed as box-and-whisker plots of density as in **Figure 2C**. Statistical significance was determined using the KS test.
D) As in (C) but sum total TOP2 CCs found in these regions.

Figure 6

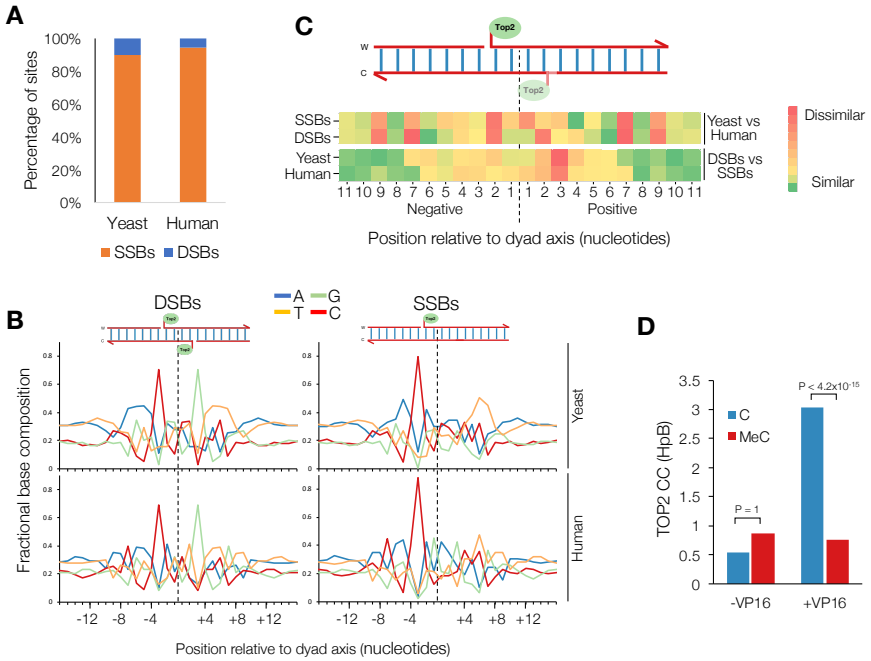

Figure 6. Local DNA sequence and methylation status direct the formation of Top2 CCs
A) The percentage of strong sites that are SSBs and DSBs in etoposide-treated *S. cerevisiae* and human cells.
B) Average nucleotide composition over a 30 bp window centred on the DSB or (inferred) SSB dyad axis, in etoposide-treated *S. cerevisiae* and human cells. Values reported are for the top strand only.
C) Heatmaps describing pairwise similarity of nucleotide composition patterns shown in (B). Rows 1-4 are the absolute differences between: yeast and human SSB patterns, yeast and human DSB patterns, yeast SSB and DSB patterns, and human SSB and DSB patterns, respectively.
D) The average number of TOP2 CCs at the +1 position relative to methylated and unmethylated cytosines in human RPE-1 cells, ±VP16. Statistical significance was determined using KS test.

Figure S1

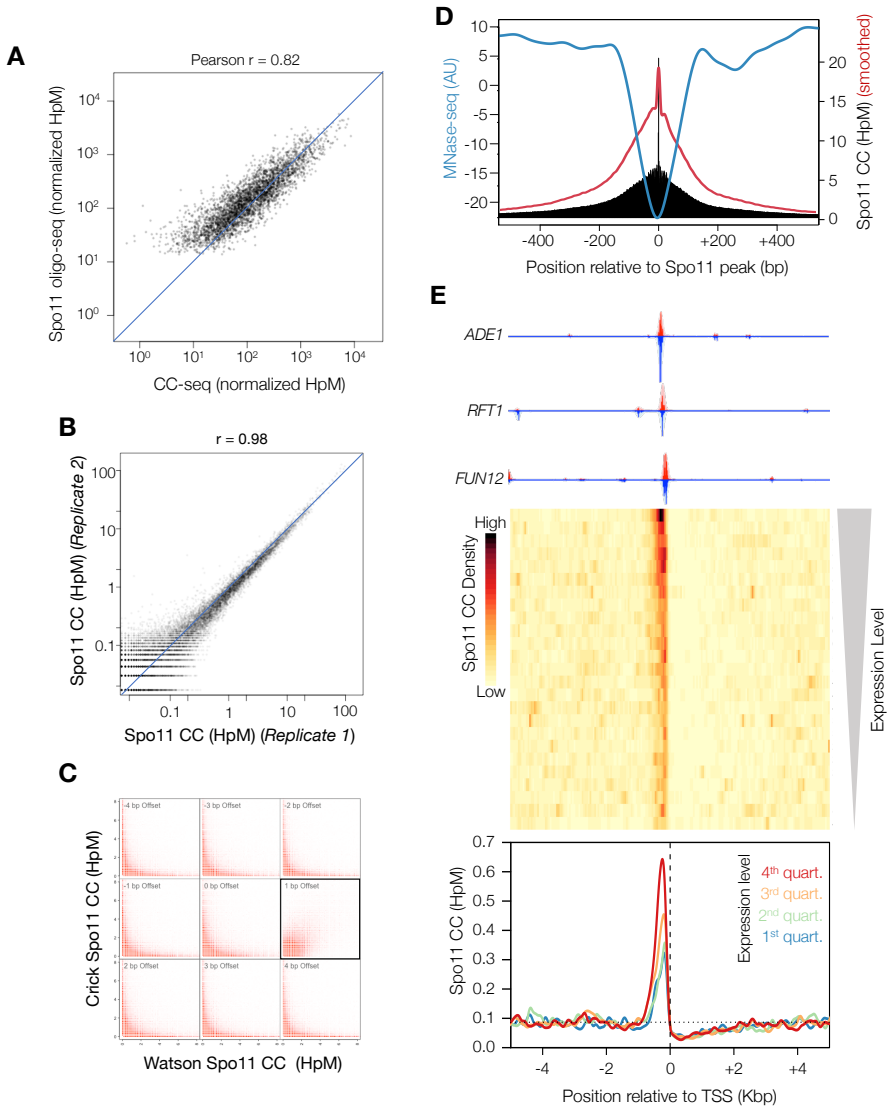

Figure S1. CC-seq maps covalent Spo11-linked DNA breaks in *S. cerevisiae* meiosis with nucleotide accuracy (related to Figure 1)

A) Correlation of hotspot signals from CC-seq and oligo-seq.

B) Correlation of 500 bp binned Spo11 maps from two representative replicates.

C) Correlation of Spo11 cleavages on Watson and Crick strand when offset by 1 bp (boxed), relative to other offsets from -4 to +4 bp.

D) Spo11 breaks mapped by CC-seq (raw=black, or smoothed=red) anticorrelate with nucleosome occupancy measured by MNase-seq (blue).

E) Aggregation of Spo11 activity in a 10 Kbp window centred on orientated TSSs in *S. cerevisiae*. Three example TSSs are shown orientated in the 5'-3' direction (top). A heatmap of all TSSs in the *S. cerevisiae* genome, with 25 rows stratified by gene expression level in SK1 cells (middle). The colour scale indicates average Spo11 break density. Motifs are also stratified into 4 quartiles of gene expression in meiotic SK1 cells, and the average distribution of Spo11 activity in each quartile plotted (bottom).

Figure S2

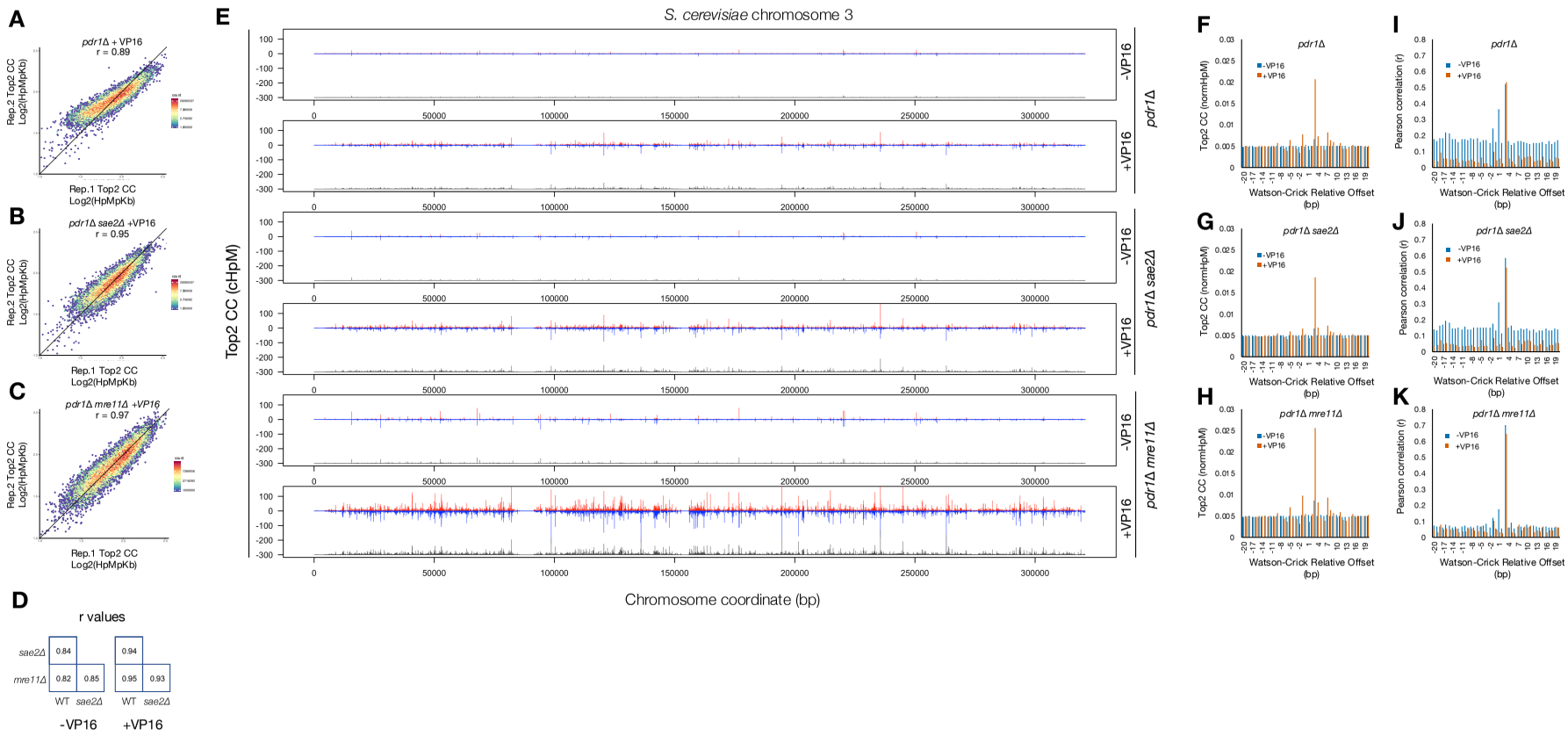

Figure S2. CC-seq maps covalent Top2-linked DNA breaks in *S. cerevisiae* cycling cells with nucleotide accuracy (related to Figure 2).
A-C) Correlation of 1 Kbp binned Top2 CC maps from *pdr1*Δ (A), *pdr1*Δ*sae2*Δ (B) and *pdr1*Δ*mre11*Δ (C) cells treated with VP16.
D) Pairwise Pearson correlation values for 100 bp binned Top2 CC maps from all assayed conditions. Each condition is a pool of two biological replicates.
E) Nucleotide-resolution *S. cerevisiae* Top2 CC map of chromosome 3 for all assayed conditions. Each condition is a pool of two biological replicates.
F-H) The normalised number of Top2 CCs retained in the *pdr1*Δ (F), *pdr1*Δ*sae2*Δ (G) and *pdr1*Δ*mre11*Δ (H) cells treated ±VP16, after filtering to include only sites offset by the given number of base pairs. All data were normalised over a -100 to +100 bp window.
I-K) Pearson correlation (r) of Top2 CC-seq signal on Watson and Crick strands, offset by the indicated distance in *pdr1*Δ (I), *pdr1*Δ*sae2*Δ (J) and *pdr1*Δ*mre11*Δ (K) cells treated ±VP16.

Figure S3

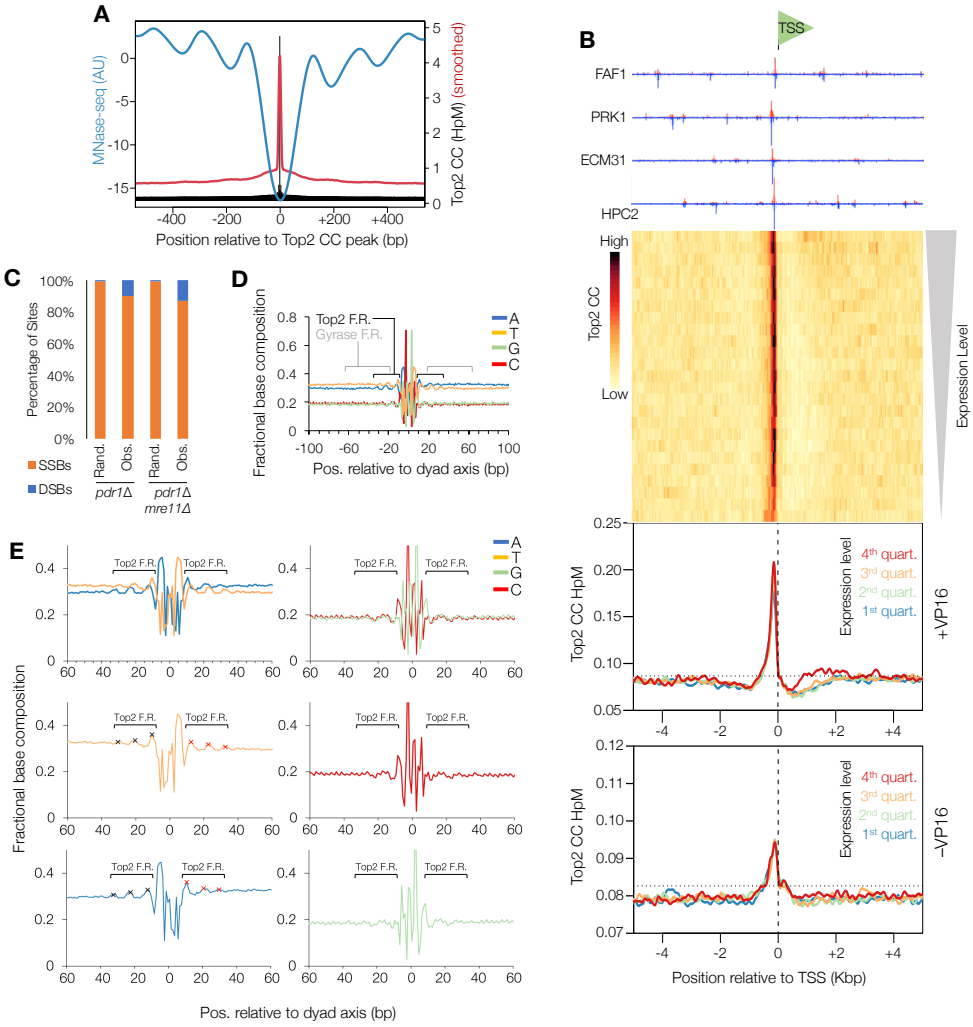

Figure S3. Top2-linked DNA breaks in *S. cerevisiae* are not correlated with gene expression, anticorrelate with nucleosomes, and have biased nucleotide skews indicative of bent DNA (related to Figure 2)

A) Top2 CC mapped by CC-seq (raw=black, or smoothed=red) anticorrelate with nucleosome occupancy measured by MNase-seq (blue).

B) Aggregation of Top2 CCs in a 10 Kbp window centred on orientated transcription start sites (TSS) in *pdr1*Δ *S. cerevisiae*. Four example TSSs are shown orientated in the 5'-3' direction (top). Heatmap of all TSSs in the *S. cerevisiae* genome, with 25 rows stratified by gene expression level in vegetative growth (middle). Colour scale indicates average Top2 CC density. Motifs are also stratified into four quartiles of gene expression, and the average distribution of Top2 CCs in each quartile plotted for untreated and +VP16 conditions (bottom).

C) The percentage of strong sites that are SSBs and DSBs in etoposide-treated *pdr1*Δ and *pdr1*Δ*mre11*Δ *S. cerevisiae*. Sites were thresholded at 1 HpM prior to sorting into DSB or SSB classes based on presence or absence of a 3 bp offset cognate (Obs.). As a control, the amplitudes of Top2 CCs (HpM) were randomised amongst the positions in the nucleotide resolution datasets, prior to thresholding and offset analysis as described above (Rand.)

D) Average nucleotide composition over a 200 bp window centred on the DSB dyad axis, in etoposide-treated *S. cerevisiae*. The position of the flanking regions (F.R.) identified in Gyrase mapping experiments, and the flanking regions observed here for Top2 are indicated in blue and black, respectively.

D) Average nucleotide composition over a 120 bp window centred on the DSB dyad axis, in etoposide-treated *S. cerevisiae*. The signal pattern is separated into A+T and G+C (top left and right), and into individual A, T, C and G plots (middle left, bottom left, middle right, and bottom right, respectively). The position of the flanking regions (F.R.) observed here for Top2 are indicated in black, and their ~10.5 bp periodicity is highlighted with black and red crosses.

Figure S4

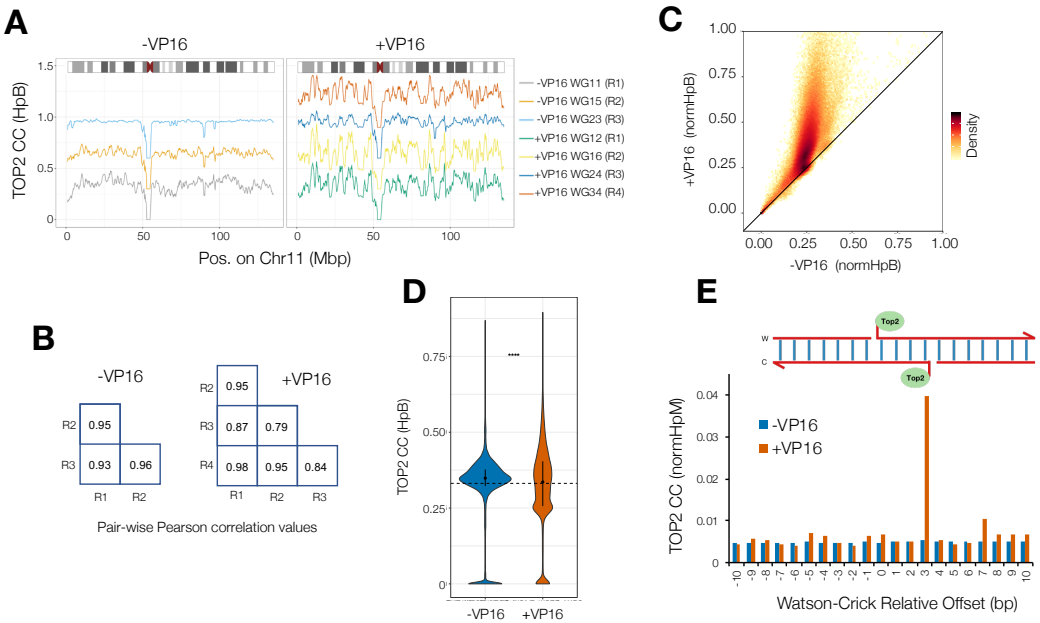

Figure S4. CC-seq maps of TOP2-linked DNA breaks in Human cells are enriched by etoposide, and show high reproducibility and nucleotide accuracy (related to Figure 3)

A) Broad-scale *H. sapiens* TOP2 CC-seq maps in individual biological replicates of RPE-1 cells ±VP16. Raw data were binned at 100 Kbp prior to plotting. Each plot is offset on the y-axis by +0.3 HpB.

B) Replicate-to-replicate Pearson correlation values (r) for 10 Kbp binned TOP2 CC-seq maps of RPE-1 cells ±VP16.

C) Scatter plot of -VP16 and +VP16 TOP2 CC-seq maps binned at 10 Kbp resolution. Data were first scaled according to the estimated noise fraction (**Methods**), and are presented in a hexagonal-binned format, where the density of overplotting is indicated by the colour scale.

D) Violin plots of TOP2 CC-seq maps ±VP16 binned at 100 Kbp resolution. The inner black bar, black dot, and dotted horizontal line indicate the interquartile range, median, and expected mean Top2 CC density based on random distribution.

E) The normalised number of TOP2 CCs retained in the CC-seq maps in RPE-1 cells ±VP16 after filtering to include only sites offset by the given number of base pairs. Data were normalised over a -100 to +100 bp window.

Figure S5

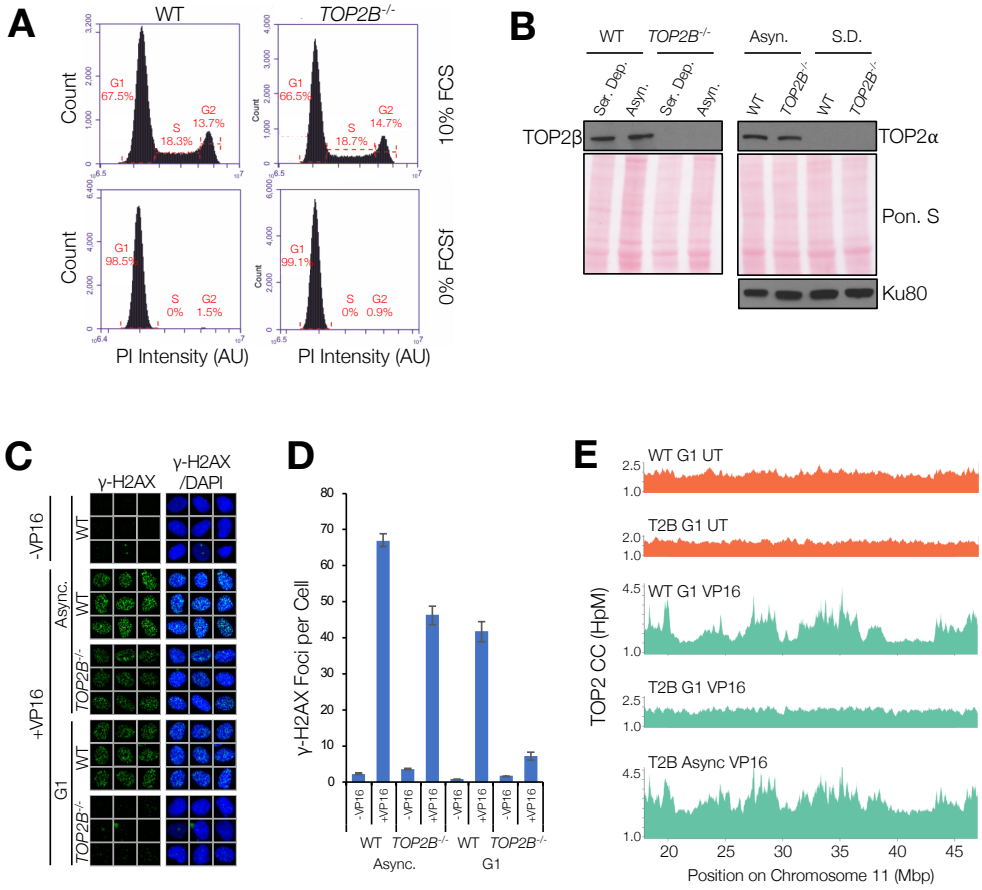

Figure S5. CC-seq signal is TOP2-dependent

A) DNA content histograms of wild type (WT) and *TOP2B*$^{-/-}$ RPE-1 cells under asynchronous (10% FCS) and serum-deprived (0% FCS) conditions, as measured by FACS following propidium iodide (PI) staining. G1, S and G2 populations are clearly present under asynchronous growing conditions. A strong G1 arrest is observed in serum deprived conditions. Percentages of cells in each of the indicated regions (red dotted brackets) are given.

B) Western blots demonstrating the absence of TOP2β protein in serum deprived and asynchronous *TOP2B*$^{-/-}$ RPE-1 cells (left), and the absence of TOP2α in serum deprived wild type and *TOP2B*$^{-/-}$ RPE-1 cells (right). Ponceau S total protein loading is presented (Pon. S) for the left and right panels, and additionally a Ku80 loading control is included for the right panel.

C) Immunofluorescence experiment demonstrating induction of γ-H2AX foci (green) in asynchronous (Async.) and serum-deprived (Ser. Dep.) wild type (WT) and *TOP2B*$^{-/-}$ RPE-1 cells, all co-stained with DAPI (blue). Galleries of nine cells per condition were chosen randomly using Olympus ScanR Analysis software.

D) Quantification of (C). Numbers of γ-H2AX foci per cell were counted automatically using Olympus ScanR Analysis software. The mean ±SEM is reported for n= 3 biological replicate experiments.

E) Broad-scale *H. sapiens* TOP2 CC-seq maps in asynchronous and serum-deprived wild type (WT) and *TOP2B*$^{-/-}$ RPE-1 cells -VP16 (orange) and +VP16 (green). Raw hits on Watson and Crick strands were summed and smoothed according to local signal density (Fsize=501).

Figure S6

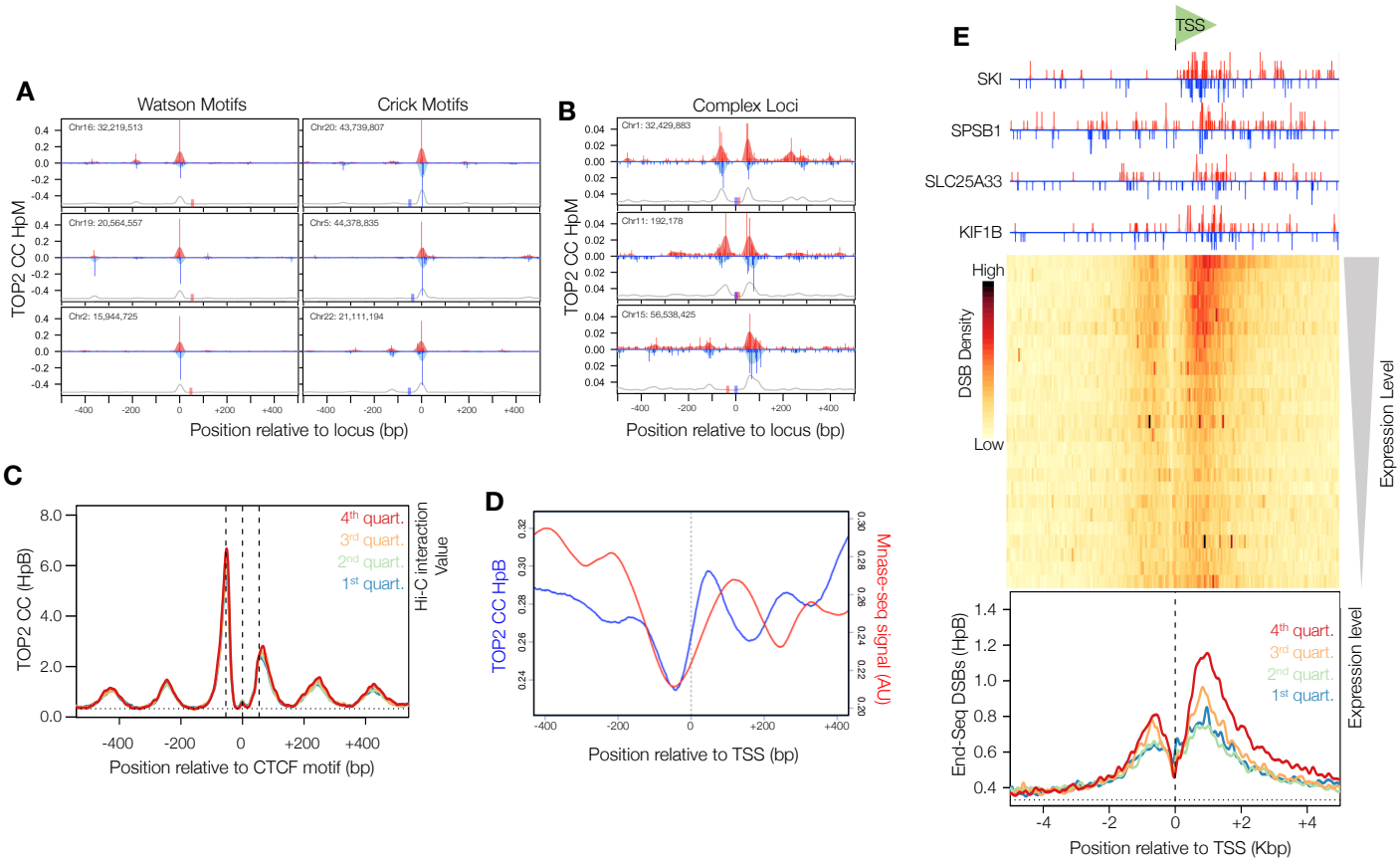

Figure S6. TOP2 CC-seq signal enrichment around CTCF and TSS sites, compared with END-seq DSB signal at TSSs

A) Fine-scale TOP2 CC-seq maps of *H. sapiens* CTCF-proximal loci in RPE-1 cells +VP16. Red and blue traces indicate TOP2-linked 5' DNA termini on the Watson and Crick strands, respectively. Pale shaded areas are the same data smoothed with a sliding 11 bp Hanning window. Red and Blue rectangles indicate the positions of CTCF motifs on the Watson and Crick strands respectively. The grey line indicates Hanning-smoothed sum of Watson and Crick TOP2 CCs.

B) Fine-scale mapping of TOP2 CCs surrounding three complex CTCF loci, processed as in (A).

C) Aggregation of TOP2 CCs in a 1 Kbp window centred on the subset of orientated CTCF motifs that can be assigned to a chromatin loop anchor in human RPE-1 cells (Darrow et al., 2016). Motifs are stratified into 4 quartiles of loop anchor interaction strength, and the average TOP2 CC distribution in each quartile plotted.

D) Fine-scale aggregation of TOP2 CCs (red) in a 800 bp window centred on TSSs in human RPE-1 cells, showing anticorrelation with aggregated MNase-seq signal (blue).

E) Aggregation of END-seq mapped DSBs in a 10 Kbp window centred on orientated TSSs in human MCF7 cells. Four example TSSs are shown orientated in the 5'-3' direction (top). A heatmap of all TSSs in the human genome, with 25 rows stratified by flanking gene expression level in MCF7 cells (middle). The colour scale indicates average END-seq DSB density. TSSs are also stratified into 4 quartiles based on strength of flanking gene expression, and the average END-seq DSB distribution in each quartile plotted (bottom).

Figure S7

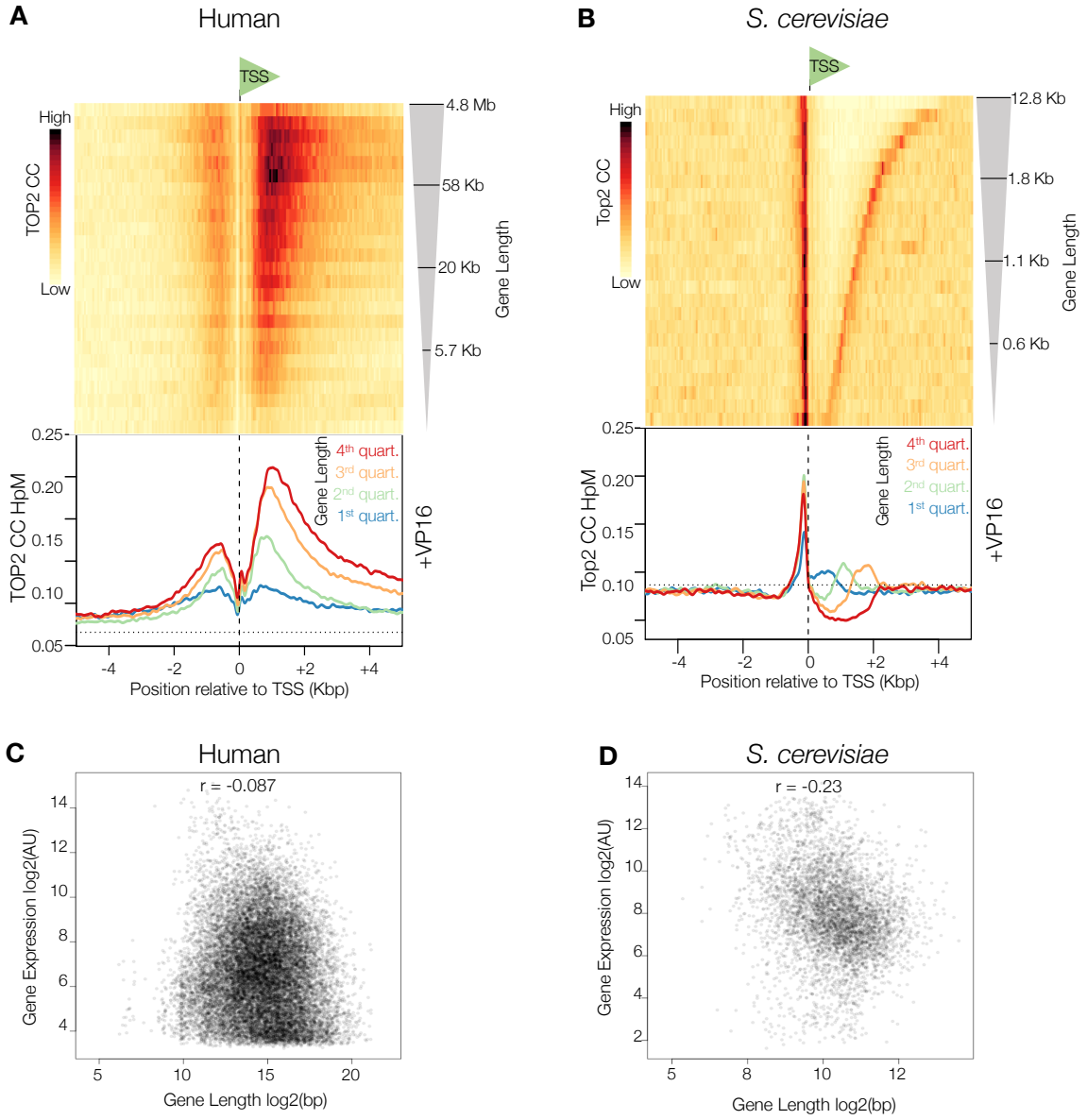

Figure S7. TSS-proximal TOP2-linked DNA breaks in humans are correlated with gene length, independently from gene expression level (related to Figure 5); TSS-proximal Top2-linked DNA breaks in yeast are not strongly correlated with gene length, (related to Figure 2)

A) Aggregation of TOP2 CCs in a 10 Kbp window centred on orientated TSSs in human RPE-1 cells. A heatmap of all TSSs in the human genome, with 25 rows stratified by gene length (top). The colour scale indicates average TOP2 CC density. Motifs are also stratified into 4 quartiles of gene length, and the average TOP2 CC distribution in each quartile plotted (bottom).

B) Aggregation of Top2 CCs in a 10 Kbp window centred on orientated transcription start sites (TSS) in *pdr1*Δ *S. cerevisiae*. Heatmap of all TSSs in the *S. cerevisiae* genome, with 25 rows stratified by gene length level (top). Colour scale indicates average Top2 CC density. Motifs are also stratified into four quartiles of gene length, and the average distribution of Top2 CCs in each quartile plotted (bottom).

C) Scatter plot of human gene length and RPE-1 gene expression, showing no correlation.

D) Scatter plot of *S. cerevisiae* gene length and gene expression during vegetative growth, showing little correlation.